

Synthesis of thin film infinite-layer nickelates by atomic hydrogen reduction: clarifying the role of the capping layer

C. T. Parzyck,¹ V. Anil,¹ Y. Wu,¹ B. H. Goodge,^{2,3} M. Roddy,¹ L. F. Kourkoutis,^{2,3} D. G. Schlom,^{3,4,5} and K. M. Shen^{1,3,6}

¹Laboratory of Atomic and Solid State Physics, Department of Physics, Cornell University, Ithaca, NY 14853, USA

²School of Applied and Engineering Physics, Cornell University, Ithaca, NY 14853, USA

³Kavli Institute at Cornell for Nanoscale Science, Cornell University, Ithaca, NY 14853, USA

⁴Department of Materials Science and Engineering, Cornell University, Ithaca, NY 14853, USA

⁵Leibniz-Institut für Kristallzüchtung, Max-Born-Straße 2, 12489 Berlin, Germany

⁶Institut de Ciència de Materials de Barcelona (ICMAB-CSIC), Campus UAB Bellaterra 08193, Spain

(Dated: January 17, 2024)

We present an integrated procedure for the synthesis of infinite-layer nickelates using molecular-beam epitaxy with gas-phase reduction by atomic hydrogen. We first discuss challenges in the growth and characterization of perovskite NdNiO₃/SrTiO₃, arising from post growth crack formation in stoichiometric films. We then detail a procedure for fully reducing NdNiO₃ films to the infinite-layer phase, NdNiO₂, using atomic hydrogen; the resulting films display excellent structural quality, smooth surfaces, and lower residual resistivities than films reduced by other methods. We utilize the *in situ* nature of this technique to investigate of the role that SrTiO₃ capping layers play in the reduction process, illustrating their importance in preventing the formation of secondary phases at the exposed nickelate surface. A comparative bulk- and surface-sensitive study indicates formation of a polycrystalline crust on the film surface serves to limit the reduction process.

Over the past four years there has been a renewed interest in the synthesis of the rare-earth perovskite and infinite-layer (IL) nickelates, spurred on by the discovery of superconductivity in the IL nickelates.¹⁻⁴ Owing to challenging synthesis conditions for nickelate single crystals^{5,6} and their subsequent reduction to the IL phase,⁷⁻¹¹ much of this work has focused on thin films; to date, superconductivity has not yet been observed in bulk, reduced nickelates. Correspondingly, there has been a recent renaissance in the study of perovskite nickelates, their metal-to-insulator transition (MIT),¹² and accompanying antiferromagnetism.^{13,14} Nonetheless, the growth and reduction of NdNiO₃ thin films are not without their own challenges. Non-stoichiometry¹⁵⁻¹⁸ and strain¹⁹⁻²¹ both substantially influence the growth and properties of the precursor phase, as well as the quality of subsequently reduced films.²² Furthermore, the typical calcium hydride reduction process employed to form the IL phase typically reduces sample crystallinity, with weaker diffraction peaks observed in reduced films than in their precursors. This degradation is at least partially attributable to the instability of Ni¹⁺ in the IL phase, which decomposes into the thermodynamically preferred 2+ state at elevated temperatures.^{23,24} As a result, long reaction times (typically hours for films and days in bulk) induce a competition between reduction and decomposition during the low-temperature second step.

In this article we discuss the *in situ* synthesis of NdNiO₂ thin films using a combined molecular-beam epitaxy and atomic hydrogen reduction system. We begin with a description of some obstacles to the growth of thin films of NdNiO₃ under high tensile strain ($\epsilon = 2.6\%$) on (001) SrTiO₃ substrates, including the confounding factors of non-stoichiometry and strain relaxation on the transport properties of precursor films. We identify a strong aging effect in the resistivity of stoichiometric films and, using a combination of x-ray diffraction (XRD) and high-resolution scanning transmission electron microscopy (STEM), demonstrate it results from post-growth strain relaxation via the formation of microscopic

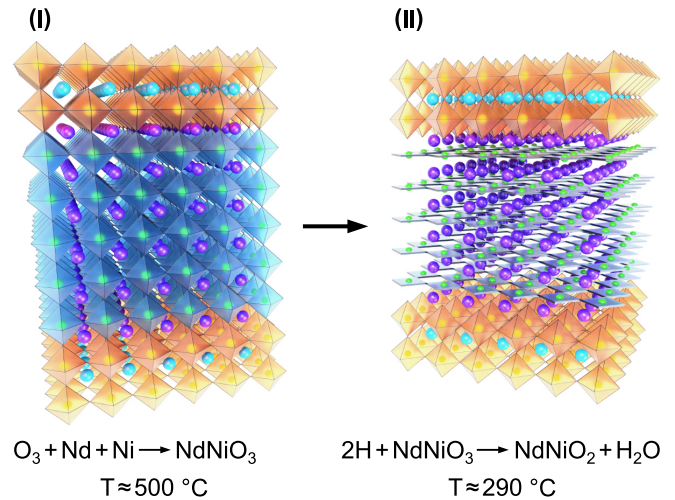


FIG. 1. Schematic of the two-step *in situ* synthesis of NdNiO₂. (I) First the perovskite NdNiO₃ film is grown using distilled ozone and molecular beams of Nd and Ni. (II) Second, the temperature is lowered and atomic hydrogen is flowed across the sample surface, scavenging oxygen from the film and topotactically reducing it to NdNiO₂. H₂O generated from this reaction is removed from the system with a high-vacuum pump.

cracks. After identifying suitable conditions for the growth of the perovskite, we introduce a novel procedure for reduction to the IL phase using an atomic-hydrogen-beam source.^{25,26} We show that topotactic reduction of NdNiO₃ to NdNiO₂ utilizing atomic hydrogen can be accomplished in short periods (< 20 minutes) and without the need to remove the films from vacuum. Structural and electrical transport measurements indicate a high degree of crystallinity and low surface roughness, establishing this method as a viable alternative to traditional direct contact reduction procedures. The amenability of this technique to integration with surface sensitive probes is

demonstrated by studying the reduction process using reflection high-energy electron diffraction (RHEED). The ability to perform surface-sensitive diffraction allows us to investigate the importance of SrTiO₃ capping layers on the reduction of nickelate films, illustrating that uncapped films suffer degradation of the film surface during the reduction. Furthermore, comparison between bulk and surface sensitive measurements indicate that the formation of this secondary-phase ‘crust’ strongly impacts the reduction process; the same reduction conditions which produce the IL phase in capped samples are insufficient to significantly reduce comparable uncapped samples. The fact that the addition of a single SrTiO₃ cap layer to a 20 u.c. thick film drastically changes the reduction rate of the whole film suggests the primary importance of the capping layer is, counterintuitively, to facilitate oxygen removal from the system.

I. SYNTHESIS OF THE PEROVSKITE PRECURSOR

Historically, nickelate thin films have been synthesized using a wide variety of techniques including pulsed-laser deposition,²⁷ off-axis magnetron sputtering,¹² and molecular-beam epitaxy (MBE);²⁸ in all cases the perovskite exhibits a strong sensitivity to composition, both in terms of the cation ratio^{15–17} and oxygen non-stoichiometry.^{19,20} We utilize reactive oxide MBE with distilled ozone (~80%) as the oxidizing agent and a shuttered growth strategy with initial shutter times calibrated using RHEED oscillations measurements of NiO and Nd₂O₃²⁹ and refined using the method described by Li et al.¹⁸ The film composition is inferred from the out-of-plane lattice constant, which has a measurable dependence on the cation ratio to the percent level (*c.f.* supplementary materials). Following this procedure we obtain a minimal out-of-plane lattice constant of 3.736 Å, from Nelson-Riley analysis,³⁰ and fully coherent films with sharp MITs. It has been shown previously that the strength and sharpness of the MIT are strongly influenced by the film non-stoichiometry;^{16,17,31} in our films, we do observe a dependence of the MIT sharpness on the cation ratio, but do not realize a complete suppression of the MIT in the neodymium rich limit (as observed in films under compressive strain^{16,31}). Comparison of the film resistivity and MIT transition temperature show monotonic dependence on the lattice constant, further evidencing it as a good metric for the film non-stoichiometry.

A. Resistivity of the Perovskite

Having tuned the cation ratio to nearly 1-to-1, we investigate the electrical properties of the resulting films. When the resistivity of a 20 pseudocubic (pc) unit cell (u.c.) film is measured within two hours following growth, Figs. 2(a), the MIT is sharp, with an upturn in the cooling curve at ~140 K followed by a hysteretic return in the warming curve at ~159 K. When the measurement is repeated, however, ~6 days later the hysteresis loop is noticeably broadened and these two temperatures are nearly coincident at an elevated value of

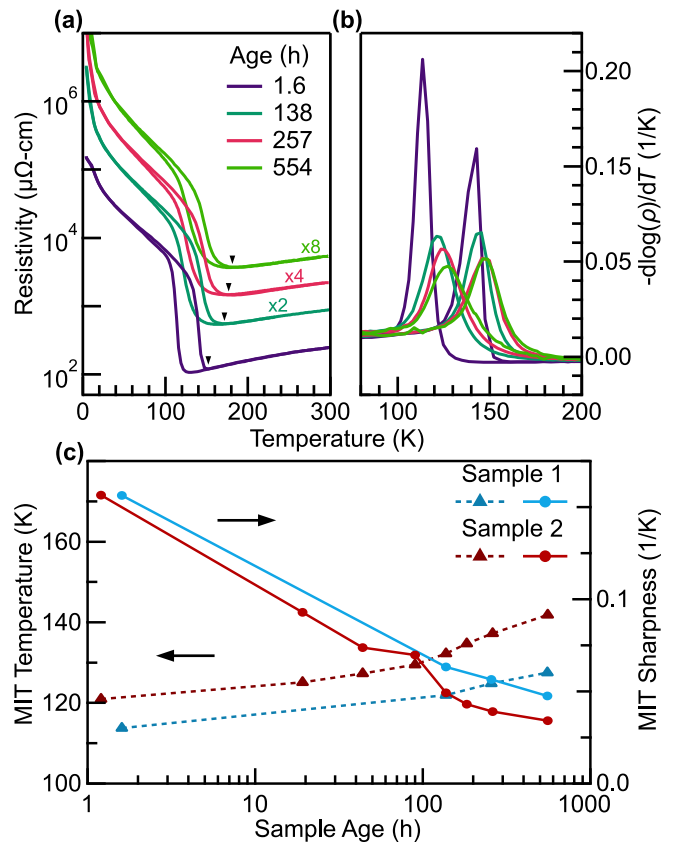


FIG. 2. Aging effects on the electrical transport properties of 20 u.c. thick NdNiO₃ films on SrTiO₃. (a) Resistivity of a 20 u.c. film measured repeatedly after its initial growth; traces have been offset for clarity. (b) Logarithmic derivative of the data from panel (a). (c) Transition sharpness and temperature, the maximum value and location of the logarithmic derivative of the resistivity, respectively, for two nominally identical samples measured at different time intervals following growth.

~170 K. Subsequent measurements show further widening of the transition, an increase of the upturn temperature to >180 K, and an increase in the room temperature resistivity. The maximum value of the logarithmic derivative of the resistivity, $(-d \log(\rho)/dT)$, gives a measure of the MIT sharpness, and its position provides an even-handed measurement of the transition temperature. Corresponding curves of the logarithmic derivatives and extracted values are shown in Figs. 2(b) and 2(c); the MIT sharpness (temperature) monotonically decreases (increases), roughly logarithmically with time. A second, nominally identical, sample was measured over the same time period but at a greater frequency and showed identical trends in the sharpness and transition temperatures, verifying that the observed effect is time-dependent rather than a byproduct of thermal cycling. While the degradation of films under such high tensile strain is not wholly unexpected, the substantial changes in the electrical properties over the course of a single day could confound (epitaxial) strain studies of the MIT in the perovskite nickelates.

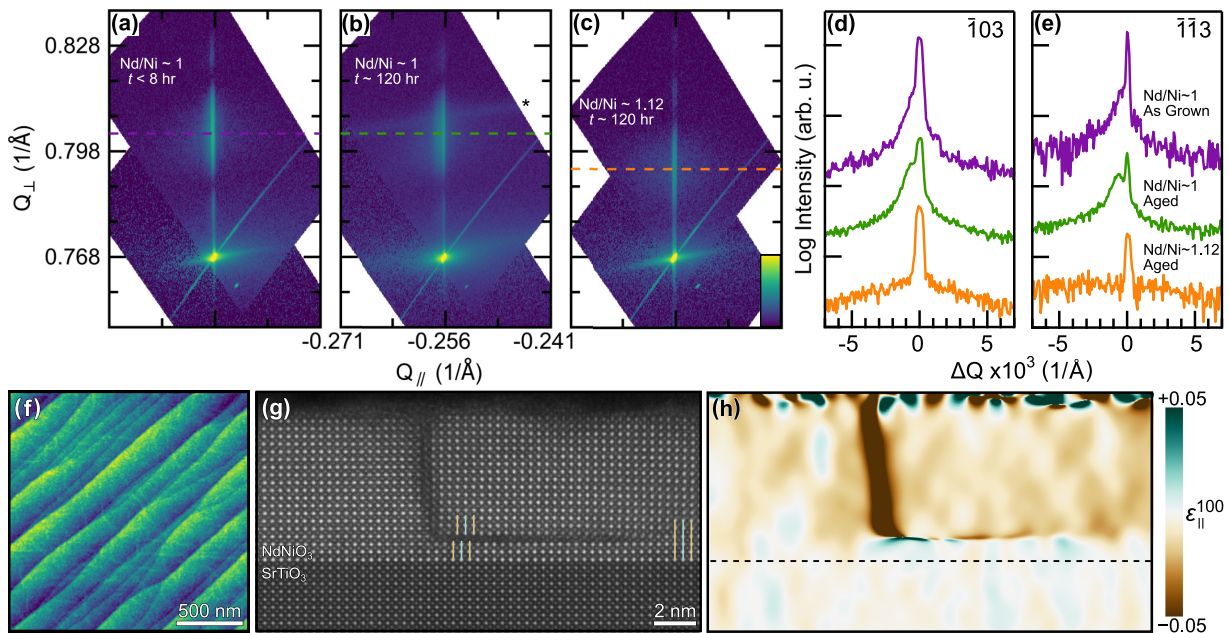


FIG. 3. Aging effects on the structure of 20 u.c. thick NdNiO_3 films on SrTiO_3 . (a) Reciprocal space map about the $\bar{1}03$ peaks of a stoichiometric film measured at a time $t < 8$ hours after growth. (b) Measurement of the same sample ~ 120 h later; (*) polycrystalline ring from residual silver paint on sample edge. (c) Measurement of a non-stoichiometric film ($\text{Nd/Ni} \approx 1.12$) 5 days following growth. (d) Line cuts from panels (a-c) at the peak maximum $\pm 2 \times 10^{-3} \text{ \AA}^{-1}$, traces offset for clarity. (e) Line cuts from equivalent positions on maps about the $(\bar{1}13)_{\text{pc}}$ peaks of the same films. (f) AFM image of an aged (> 1 week) NdNiO_3 sample showing striations. (g) High-angle annular dark-field image of a crack and resulting delamination in a 3-day-old sample; lines highlight columns of Nd atoms, which should be continuous. (h) Map of in-plane compressive strain in (g) highlighting local changes in the lattice fringe spacing.

B. Post-growth Structural Relaxation

In Fig. 3, we show that the observed changes in resistivity are attributable to post growth strain relaxation by way of crack formation. A reciprocal space map (RSM) about the $(\bar{1}03)_{\text{pc}}$ reflection of a stoichiometric film, measured immediately following growth, shows a sharp peak aligned with the substrate; upon repetition of the measurement 5 days later, a significant shoulder is apparent. When a purposefully neodymium rich film ($\text{Nd:Ni} \sim 1.12$) is measured 5 days following growth, however, no shoulder is observed, indicating the film remains coherent. This, and equivalent data about $(\bar{1}13)_{\text{pc}}$ summarized in Figs. 3(d) and 3(e), are consistent with fully coherent as-grown films, regardless of the cation non-stoichiometry. Nonetheless, films with $\text{Nd:Ni} \sim 1$ do not maintain coherence on the hour timescale. Instead, they form regions with a smaller in-plane lattice parameter: $a_{\text{pc}} \sim 3.891(5)$ – intermediate to the substrate (3.905 \AA) and bulk³² (3.807 \AA) parameters. Partial relaxation towards the bulk-like structure explains the time dependent increase in the MIT temperature, towards that of the bulk compound. The fact that neodymium-rich films do not form relaxed regions suggests the presence of Ruddlesden-Popper (RP) faults, identified in Nd rich films,²² contribute to the accommodation of both off-stoichiometry as well as high tensile strain.

Real-space probes including atomic force microscopy (AFM) and STEM reveal relaxation in the film is accomplished by crack formation and subsequent partial delamina-

tion. AFM of an aged, stoichiometric film, Fig. 3(f), shows terraces decorated with raised striations running along and across the step edges, indicative of cracking and subsequent delamination, as observed prior in perovskite oxides under biaxial tensile strain.³³ This partial delamination is directly visible by atomic-resolution HAADF-STEM imaging in Fig. 3(g) where the top surface of the film is slightly raised on one side of the crack's vertical extension. In addition to the vertical lifting of the atomic layers, in-plane relaxation above the crack can be identified by Nd atomic columns, which are offset above and below the horizontal extension (cyan and yellow lines) and by a small effective compression of the in-plane lattice fringe spacing³⁴ (light brown) in Fig. 3(h). In addition to the aforementioned time dependence in electrical transport caused by partial relaxation, the formation of extended defects may present a challenge in the reproducibility of reduction experiments. If the time between growth and reduction is not controlled, as the off-stoichiometry of the parent phase is reduced and frequency of RP faults diminished, the quality of the corresponding reduced films may become difficult to predict.

II. REDUCTION TO INFINITE-LAYER NdNiO_2

Having established conditions for synthesis of the perovskite, we introduce a novel reduction procedure to transform it to the infinite-layer phase. Traditionally, low-

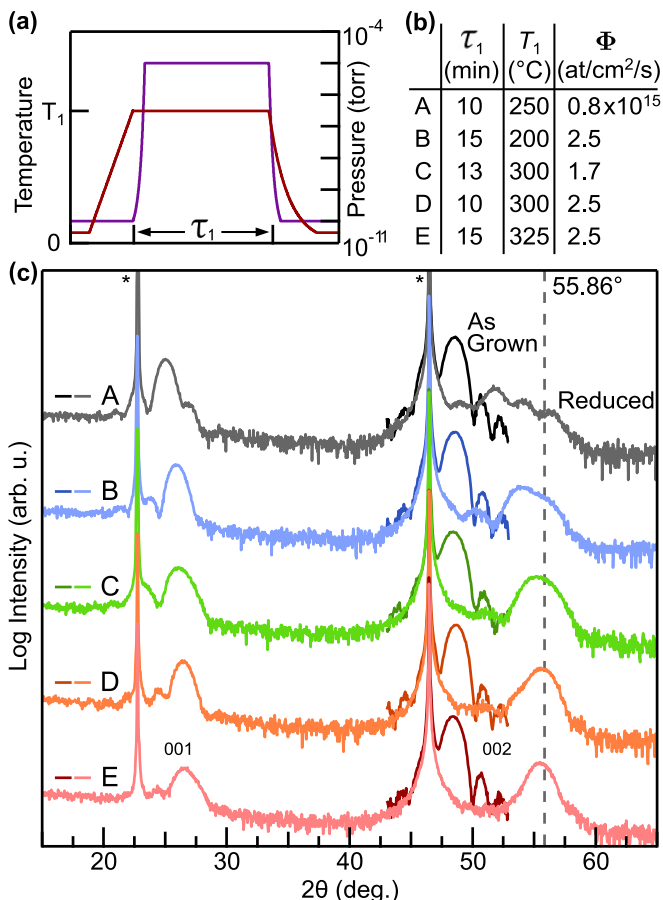


FIG. 4. Single temperature topotactic reduction of $\text{NdNiO}_3/\text{SrTiO}_3$ with atomic hydrogen. (a) Schematic of reduction procedure at a single temperature T_1 for a duration τ_1 . (b) Time, temperature, and flux conditions for reduction of samples shown in (c). (c) X-ray diffraction of a series of samples before (dark) and after (light) reduction, offset for clarity. All samples were capped with 1-3 layers of SrTiO_3 . (*) indicates reflections arising from the SrTiO_3 substrate.

temperature topotactic reduction of nickelates utilizes alkali or alkaline earth hydride powders (CaH_2 , NaH) as reducing agents. This process was introduced in studies of intermixed polycrystalline samples,^{23,24,35,36} later applied to films,^{37–39} and most recently has been refined for the production of superconducting alkaline-earth (AE) doped rare-earth (RE) nickelates, $(\text{RE},\text{AE})\text{NiO}_2$.^{1,2,22,40–42} Despite the success of this method there are a few drawbacks. Primarily, it is limited to *ex situ* use – the film needs to be removed from the growth chamber and placed in an environment with the powder, annealed, and then the reaction products removed. Often, the sample is embedded in the powder⁴³ (though there have been reports of non-contact reduction^{7,44,45}), which is not amenable to surface sensitive measurements, including scanning tunneling microscopy and photoemission spectroscopy. These techniques, fundamental to understanding the cuprates, remain uncommon in the infinite-layer nickelates.^{46–48} Additionally, long reduction times (typically hours for thin films and days for single crystals) may be detrimental to preserva-

tion of crystallinity as bulk studies indicate extended exposure to temperatures exceeding $200\text{ }^{\circ}\text{C}$ results in decomposition or disproportionation of the metastable structure.^{8,23,24} We note that there has been a recent push to identify new reduction methods for nickelates, and reduction by application of an aluminum getter layer to the film surface has been recently demonstrated.^{49,50} Similar to the recently identified solid-state aluminum reduction technique, the method described here can be achieved in the same vacuum system as the sample growth.

The use of atomic hydrogen as a powerful reducing agent has been recognized previously;⁵¹ however, to date its use has primarily been consigned to surface etching⁵² and cleaning,^{53,54} with some work on the reduction of binary oxides,^{55–57} or generation of oxygen vacancies in more complex oxides.⁵⁸ We find that exposure to an atomic hydrogen flux of $\sim 2 \times 10^{15}$ $\text{at}/\text{cm}^2/\text{sec}$ for < 15 minutes at sample temperatures between 250 and $300\text{ }^{\circ}\text{C}$ is sufficient to transform ~ 7.5 nm thick perovskite films to the IL phase, a much shorter exposure compared to traditional CaH_2 annealing.⁵⁹ We further demonstrate that this procedure produces IL films with high structural quality, smooth surfaces, and favorable electrical characteristics. Finally, we leverage the compatibility of this technique with *in situ* probes, namely RHEED, to study the effects of atomic and molecular hydrogen exposure on the film surface and the resulting impact on the reduction process.

A. Single Temperature Reduction

Following growth, 20 u.c. thick nickelate films are capped with 2-3 unit cells of SrTiO_3 and transferred, in ultra-high vacuum, to a connected chamber ($P_{\text{base}} < 1 \times 10^{-10}$ torr) with a heated sample stage. There, atomic hydrogen is generated from a thermal source^{25,26} by passing molecular H_2 through a heated tungsten capillary ($> 1900\text{ }^{\circ}\text{C}$) located 9 cm from the sample. It dissociates (with an efficiency, α , between 50 and 80%)⁶⁰ before interacting with the sample surface, scavenging O_2 from the film, and forming H_2O , which is removed via a turbomolecular pump. A schematic of a single-temperature reduction program, with typical parameters, is shown in Figs. 4(a) and 4(b); lab-based XRD measurements before and after reduction are detailed in Fig. 4(c). At low reaction times, temperatures, and fluxes (samples A, B) the perovskite transforms partially to the IL phase with a pair of additional intermediate peaks visible at $2\theta = 51.8^{\circ}$ ($c \sim 3.53\text{ \AA}$) and $2\theta = 54.0^{\circ}$ ($c \sim 3.39\text{ \AA}$), attributable to oxygen-deficient perovskite phases with partially collapsed structures. As the reaction temperature is increased from 250 to $\sim 300\text{ }^{\circ}\text{C}$ and the flux from < 1 to 2.5×10^{15} $\text{at}/\text{cm}^2/\text{sec}$ (by varying the capillary temperature and H_2 flow rate) the intermediate phase peaks are suppressed in favor of a single peak above $2\theta = 55^{\circ}$, indicative of the IL phase (Sample E). Eliminating these oxygen-rich phases from NdNiO_2 samples is of paramount importance to studies targeted to understanding of the parent state from which superconductivity emerges. Excess interstitial oxygen tends to form ordered structures in all members of the RENiO_2 , $\text{RE}=\text{La, Pr, Nd}$, family.^{11,61–67} In-

clusions of these phases may serve to confound resonant scattering studies, which are highly sensitive to periodic valence modulations of the nickel.⁶⁸

B. Three-Step Reduction

While the single temperature reduction procedure is shown to effectively produce the IL phase, the resulting films have reduced crystallinity compared to the perovskite, evidenced by reduction in the (002) Bragg peak intensity. We quantify the conversion efficiency from the perovskite to the IL phase by the ratio of the (002) peak intensity before (I) and after (I') reduction: $R_{002} = I(2\theta = 48.71^\circ)/I'(2\theta = 55.86^\circ)$. Owing to changes in the structure factor, some decrease in intensity is expected: the optimal (*i.e.* minimal) value of R_{002} is calculated to be 1.58 using a dynamical diffraction model.⁶⁹ For reference, the value of R_{002} , for sample E in Fig. 4(b) is 13.1. This discrepancy highlights that although the reduction may proceed across the entire thickness of the film (evidenced by the Scherrer thickness from the 002 peak) the coherent crystalline volume of the reduced film is reduced from that of the perovskite.

To further improve the crystallinity, we perform a three-step reduction procedure utilizing the independent control of the sample temperature and reducing atmosphere afforded in this setup. Outlined in Fig. 5(a) and 5(b), the procedure consists of: (1) heating close to the reduction temperature ($\sim 250^\circ\text{C}$) in vacuum for 8 minutes to achieve thermal equilibrium; (2) the hydrogen flow is turned on and the sample exposed to the atomic H beam for 6-8 minutes as the flow rate stabilizes; (3) the sample is quickly heated to the final temperature for a short period, typically 3-5 minutes, before terminating the hydrogen flow and cooling the sample. As illustrated in the corresponding XRD measurements, Fig. 5(c), using similar parameters to those in Fig. 4 results in similar values of R_{002} (Sample A'). Lowering the reduction time while increasing the temperature and flux appears to improve the conversion efficiency; with full reduction achievable in only 10-12 minutes of total exposure time (Sample C' - E'), with an optimized value of $R_{002} \approx 6$ in sample C'. The precise value of the high-temperature step does not appear to strongly influence R_{002} ; this is possibly attributable to the short duration of the final step, during which the sample surface may not fully equilibrate to the heater. Although the conditions of sample C' provide the best conversion efficiency, Fig. 5(b) illustrates that the IL phase can be isolated over a reasonable window of times, temperatures, and fluxes.

Further structural characterization is outlined in Fig. 5(d)-5(f). X-ray reflectivity (XRR) of a film is measured immediately after growth and then again following capping with 2 u.c. of SrTiO₃ and reduction. The thickness and roughness of the NdNiO_x slab obtained from a dynamical fit of the XRR⁶⁹ are $\ell_{PER} = 7.31$ nm, $\sigma_{PER} = 0.5$ nm before the reduction and $\ell_{IL} = 6.20$ nm, $\sigma_{IL} = 1.9$ nm after. The thickness ratio of $\ell_{IL}/\ell_{PER} = 0.85$ matches the ratio of the c -axis lattice constants, 0.88 – consistent with a full collapse of the structure without substantial increase in the sample

roughness. An RSM about the $\bar{1}03$ peaks of SrTiO₃ and NdNiO₂ shows that coherence of the film is maintained through the reduction process. In a 00L scan of a 3 u.c. SrTiO₃ capped film (supplemental materials) all of the 001 through 004 reflections are visible in the IL film, and an out-of-plane lattice parameter of $c = 3.286$ Å is calculated from Nelson-Riley analysis,³⁰ in good agreement with previous measurements of chemically reduced films.^{40,70} A simulation of unreduced NdNiO₃/SrTiO₃ is fit to the XRD data in Fig. 5(f) to extract the setup parameters, which are then used to simulate the XRD for an NdNiO₂ film (changing only the structure from NdNiO₃ to NdNiO₂). Comparing to a capped/reduced film, the observed pattern of Pendellösung fringes (and the Scherrer thickness) are correctly reproduced in the simulation, including the fringe spacing and the asymmetric intensity pattern.

C. Electrical Transport Measurements

The resistivity of a representative set of films reduced using the three-step procedure is shown in Fig. 6. Transport measurements of films, with varying cap thickness, show residual resistivities between 300 and 600 $\mu\Omega\text{-cm}$; this is lower than comparable undoped nickelate films on (001) SrTiO₃^{40,42,49} and comparable to underdoped films reported on (001) LSAT^{50,71} prepared by other methods. All samples show some degree of an upturn at low temperature, between 20 and 35 K. Hall measurements, detailed in Fig. 6(b), show a flat temperature dependence of R_H between 75 and 300 K, consistent with prior measurements on undoped and underdoped NdNiO₂,^{38,40,41} accompanied by a downturn at low temperature. The Hall coefficient, R_H , in the high temperature limit is around -0.01 cm³/C, which is intermediate to prior measurements of films on SrTiO₃, between -0.005 reported by Li et al.⁴⁰ and -0.035 as reported by Zeng et al.⁴¹ In contrast to prior measurements, a slight upturn in R_H is visible below 25 K. However, we note that the precise shape of $R_H(T)$ reported in the literature appears to vary considerably between different samples,^{40,41} A-site cations,⁴² and strain states.⁷¹

D. Effects of the Capping layer

We conclude with a study of the effects of molecular and atomic hydrogen on film surfaces during reduction. Earlier reports have speculated on the role of the capping layer during reduction; our experiments reveal that exposure of the nickelate surface to a reducing atmosphere results in the formation of a polycrystalline scale layer on the sample surface. Furthermore, uncapped samples with this scale layer are *not* reduced under the same conditions which are sufficient for reduction of films capped with caps as thin as 1 u.c. of SrTiO₃. In previous sections we have described samples capped with 1-3 u.c. of SrTiO₃ and reduced with atomic hydrogen. Here we describe what happens to films without a capping layer when they are exposed to H and H₂. Figure 7(a) displays XRD of a series of 20 u.c. thick films (capped and uncapped) following expo-

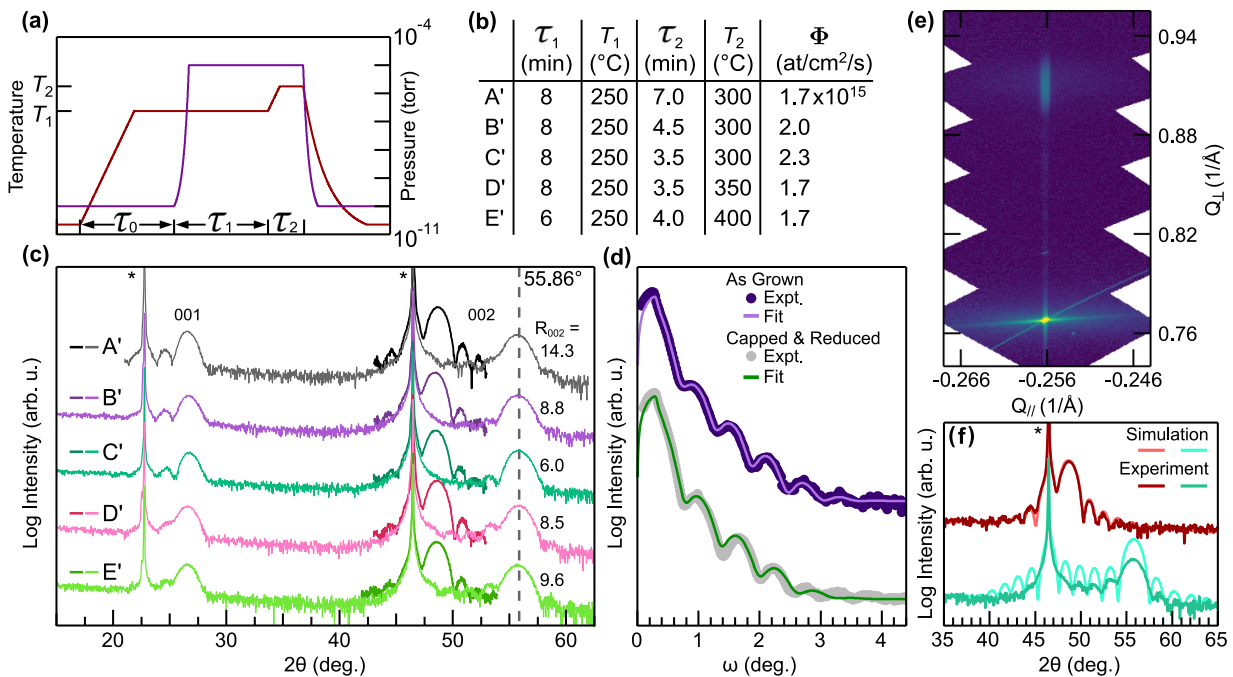


FIG. 5. Structural characterization of optimally reduced $\text{NdNiO}_2/\text{SrTiO}_3$. (a) schematic of the three-step reduction procedure. (b) Parameters used in the reduction of samples in (c); in all pictured cases an initial equilibration time of $\tau_0 = 8$ minutes was used. (c) XRD of samples before (dark) and after (light) reduction. The ratio of the 002 peak intensity before and after reduction ($R_{002} = I(2\theta = 48.71^\circ)/I'(2\theta = 55.86^\circ)$) is shown as a metric of the conversion efficiency. (d) X-ray reflectivity of the same sample immediately after growth (black) and after capping with 2 u.c. of SrTiO_3 and reduction using the optimal conditions of C'. (e) Reciprocal space map about the $\bar{1}03$ peaks of SrTiO_3 and NdNiO_2 for a sample reduced under the optimized conditions. (f) XRD, about the 002 reflection, of representative, optimized NdNiO_3 and NdNiO_2 films with simulated diffraction patterns overlaid. (*) indicates reflections arising from the SrTiO_3 substrate.

sure to molecular or atomic hydrogen under similar conditions (chamber pressure and substrate temperature). Corresponding RHEED measurements for selected samples are included in Figs. 7(b)-7(e) and the specific details of each program are provided in the supplemental materials. Exposure of an uncapped sample to molecular hydrogen for a short duration (< 15 min) at a flux of 1.5×10^{15} $\text{H}_2/\text{cm}^2/\text{sec}$ produces no apparent change in the XRD. However, the half-order streaks (associated with rotation of the NiO_6 octahedra) are diminished, indicating a change in the surface oxygen stoichiometry. 15 minutes of additional exposure produces $1/3^{\text{rd}}$ order peaks, and with further reduction the disappearance of film peaks and formation of a secondary phase are observed. This degradation of the surface occurs at timescales short compared to the reduction of the entire film, evidenced by the modest shift in the XRD. Additionally, the total exposure of the film surface to H_2 gas in this experiment is low, limited to $< 10^6$ Langmuir (L) over 90 minutes, compared to hydride annealing experiments where the sample environment may contain up to 100 mtorr of hydrogen⁴¹ (liberated from CaH_2 or $\text{Ca}(\text{OH})_2$ ^{44,72}) for several hours ($\sim 10^9$ L).

This surface degradation also affects oxygen removal during the atomic hydrogen reduction. When an uncapped film is reduced using the three-step process with nominally optimized conditions (12 minutes of total exposure) we observe a clear degradation of the RHEED pattern: the film peak intensity is reduced, background intensity increased, and faint

polycrystalline rings appear. Surprisingly, this exposure does not produce an IL film; instead, a pair of intermediate phase peaks are observed at 2θ values of 50.1° and 52.3° . The addition of a capping layer greatly changes the process: using nearly identical time, temperature, and flux conditions, films with 1-3 layers of SrTiO_3 are reduced to the IL phase. In the 1 u.c. thick SrTiO_3 capped film, additional peaks are visible at positions not associated with Pendellösung fringes for this thickness film. These peaks, matching the positions of those in the uncapped film, suggest trace intermediate phases may remain; which are absent in the films capped with 2 or 3 u.c. of SrTiO_3 . RHEED measurements show the capped films maintain an ordered surface and AFM (supplementary materials) indicates a smooth, terraced surface is maintained, with a terrace-averaged roughness of only 1.2 Å. The substantial difference in oxygen removal between capped and uncapped films, under the same reduction conditions, highlights the cap's importance in facilitating the reduction process.

These extremely thin capping layers, approaching a single unit cell, likely do not substantially contribute to maintaining the structural stability across the entirety of the 20 u.c. film; yet they substantially influence the conditions required to reduce the film. This suggests that the cap plays a role beyond that of a simple structural support and has a substantial impact on how easily oxygen is removed from the film. This distinction can be further explored by comparing the reduction of a sample capped with 3 u.c. of crystalline SrTiO_3 with one

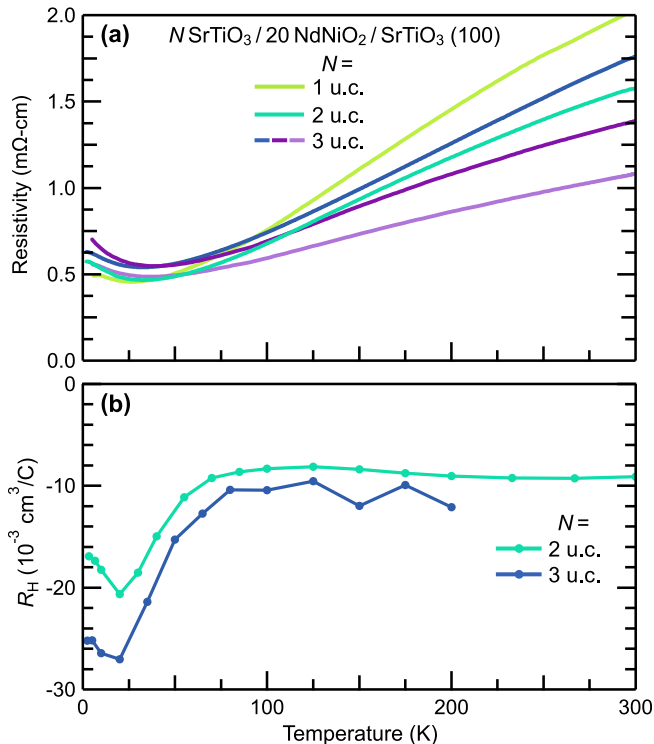


FIG. 6. Electrical transport measurements of reduced nickelate films. (a) Resistivity of representative reduced films with different SrTiO₃ cap thicknesses, N , reduced using the optimized three-step procedure. (b) Hall measurements of NdNiO₂ films capped with 2 or 3 u.c. SrTiO₃.

capped with 1.2 nm of amorphous SrTiO₃. We observe (*c.f.* Fig. 7(a)) that samples capped with amorphous SrTiO₃ are well reduced using the three-step atomic hydrogen reduction procedure, even though the cap does not provide additional epitaxial support to the film. While films with either crystalline or amorphous SrTiO₃ caps are both reduced under similar conditions, there are some slight differences in the quality of the resulting IL films – discussed in the supplemental materials – with amorphous SrTiO₃ capped films suffering from reduced crystallinity. The similarity between samples capped with crystalline and amorphous material, contrasted with the distinct behaviour of uncapped samples, strongly suggests that during the atomic hydrogen reduction the primary function of the cap is to prevent the formation of a nickelate scale layer at the sample surface, rather than providing epitaxial stabilization of the IL phase. The contrast illustrated here may help to explain observed discrepancies between capped and uncapped IL nickelate films in recent transport⁴³ and scattering⁷³ studies.

III. CONCLUSIONS

Here, we have described a novel, flexible synthesis method for IL nickelate films – one which requires only gas phase reactants and is easily integrable with thin film growth tech-

niques and surface sensitive probes. Characterization of the resulting films shows this method reproducibly yields IL films with high crystallinity, low resistivity, and flat surfaces. Utilizing the *in situ* nature of this procedure, we have investigated the effects of the reduction on the film surface to elucidate the impact of capping layers on the reaction. We find that the addition of an ultrathin cap, down to 0.4-1.2 nm, drastically improves the reduction process and inhibits the formation of a polycrystalline scale layer on the sample surface. Additionally, we have demonstrated the growth of high quality films of NdNiO₃ by MBE and illustrated that the structural and electrical characteristics of the highly strained perovskite are unstable on the timescale of hours to days. Diffraction and real-space probes indicate that the sample strain is partially relieved by the rapid formation of cracks soon after growth. These measurements indicate that care must be taken when investigating the details of the MIT in highly strained nickelates as well unveiling a potentially uncontrolled variable in nickelate reduction experiments. Topotactically reduced oxides have proven to be a rich, expanding field for the investigation of novel ground states in quantum materials;^{1,23,35,59,74-81} we put forth atomic hydrogen reduction as a highly tunable process for synthesizing reduced oxides of high quality. The vacuum compatibility of this technique both expands the range of experiments which may be performed on reduced films and enables *in situ* and *operando* studies of the reduction process itself.

IV. METHODS

Sample Growth & Characterization

Thin films of NdNiO₃ were grown on (001)-oriented SrTiO₃ substrates using reactive-oxide molecular-beam epitaxy in a Veeco GEN10 system from elemental beams of Nd (Alfa/AESAR, 99.9%) and Ni (Alfa/AESAR, 99.995%) with typical fluxes of $0.8\text{-}1.2 \times 10^{13}$ at/cm²/sec. Substrates were etched to prepare a TiO₂ terminated surface⁸² and annealed prior to growth at 650 °C until a clear RHEED pattern was observed. Growths were performed at substrate temperatures between 480 and 500 °C, measured by optical pyrometry at a wavelength of 1550 nm, in background pressures between 2 and 7×10^{-6} torr of $\sim 80\%$ distilled ozone. Following growth, samples were cooled to < 100 °C in a pressure of $> 1 \times 10^{-6}$ torr of ozone to discourage the formation of oxygen vacancies.

Structural quality and phase purity were determined using Cu K α_1 x-ray diffraction measurements performed on a PANalytical Empyrean X-ray diffractometer. Morphology was assessed using an Asylum Research Cypher environmental atomic force microscope. Electrical transport measurements were performed using both a custom built LHe-cooled four-point probe measurement station and a Quantum Design physical property measurement system utilizing either built-in electronics or a Keithley 6221 current source and 2182A voltmeter in a delta mode configuration. Geometric factors in the resistivity were accounted for using the methods of Miccoli et al.⁸³ Hall measurements were performed either over the en-

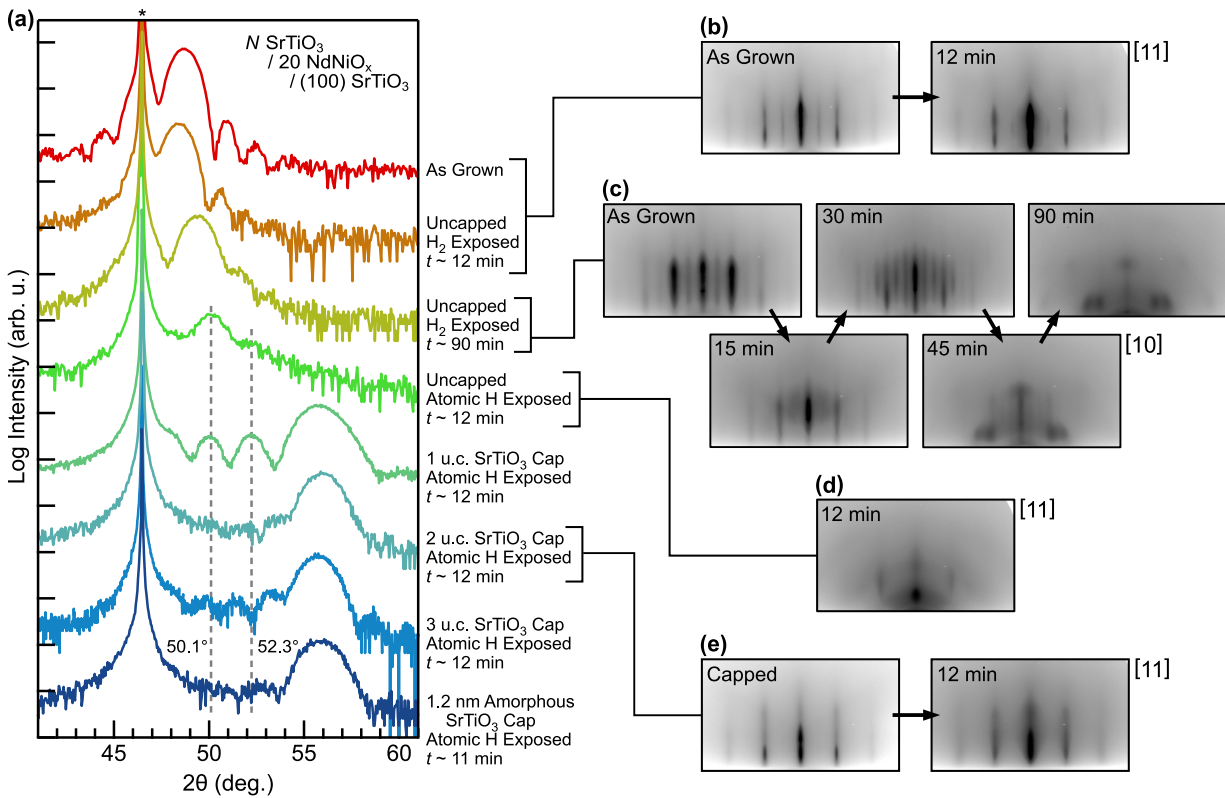


FIG. 7. Surface- and bulk-sensitive structural measurements of NdNiO_{3-x} films reduced using molecular and atomic hydrogen. (a) XRD of capped and uncapped nickelate samples exposed to molecular or atomic hydrogen. Dashed lines indicate the position of peaks likely derived from intermediately reduced phases and (*) indicates reflections arising from the SrTiO₃ substrate; traces have been vertically offset for clarity. (b) RHEED images, taken with the electron beam along the [110]_{pc} azimuth, of an uncapped perovskite film before and after a short exposure to molecular hydrogen. (c) RHEED images, taken with the electron beam along the [100]_{pc} azimuth, of an uncapped film progressively exposed for longer periods, up to a total time of 1.5 hours. (d) RHEED images, taken with the electron beam along the [110]_{pc} azimuth, of an uncapped film exposed for a short duration to atomic hydrogen. (e) RHEED images, taken with the electron beam along the [110]_{pc} azimuth, of a film capped with 2 u.c. of SrTiO₃ exposed to atomic hydrogen. All RHEED images use a logarithmic intensity scale. Samples were reduced under similar conditions with chamber pressures of $\sim 9 \times 10^{-5}$ torr and sample temperatures between 300 and 400 °C. Precise values of the times, temperatures, and fluxes used for each sample are tabulated in the supplementary materials.

tire 10×10 mm sample in a square four-point Van der Pauw configuration or using a 6-wire Hall bar geometry on a diced 5×10 mm piece.

Scanning Transmission Electron Microscopy

Cross-sectional specimens were prepared using the standard focused ion beam (FIB) lift-out process on a Thermo Fisher Scientific G4 UX FIB. HAADF-STEM images were acquired on an aberration-corrected FEI Titan Themis operating at 300 kV with a probe-forming semi-angle of 21.4 mrad and inner (outer) collection angles of 68 (340) mrad. To avoid possible image distortions from sample drift or other mechanical instabilities, all images presented here are produced by summing a stack of 50 high-frame-rate images aligned by rigid registration.⁸⁴ A small-angle shear transformation was applied to all images to correct for subtle non-orthogonality in the STEM scan. Lattice relaxation in the film was mapped with strain analysis based on a phase lock-in approach.³⁴

SUPPLEMENTARY MATERIAL

See the supplementary material for additional details about the stoichiometric calibration process, further data on the effects of non-stoichiometry and strain relaxation on transport measurements, and additional details about the effects of the reduction process on capped and uncapped films.

ACKNOWLEDGMENTS

This work was primarily supported by the National Science Foundation through Grants No. DMR-2104427 and the Platform for the Accelerated Realization, Analysis and Discovery of Interface Materials (PARADIM) under Cooperative Agreement No. DMR-2039380. Additional support was provided by the Air Force Office of Scientific Research (Grant No. FA9550-21-1-0168) and the Gordon and Betty Moore Foundation's EPIQS Initiative through Grant Nos. GBMF3850 and GBMF9073. The authors acknowledge the use of fa-

cilities and instrumentation supported by NSF through the Cornell University Materials Research Science and Engineering Center DMR-1719875. The FEI Titan Themis 300 was acquired through No. NSF-MRI-1429155, with additional support from Cornell University, the Weill Institute, and the Kavli Institute at Cornell. The Thermo Fisher Helios G4 UX FIB was acquired with support by NSF No. DMR-1539918. Substrate preparation was performed, in part, at the Cornell NanoScale Facility, a member of the National Nanotechnology Coordinated Infrastructure (NNCI), which is supported by the National Science Foundation (Grant NNCI-2025233). The authors would like to thank Sean Palmer and Steven Button for their assistance in substrate preparation as well as Hari Nair and Jiabin Sun for their thoughtful discussions and insightful comments.

AUTHOR DECLARATIONS

Conflict of Interest

The authors have no conflicts to disclose

Author Contributions

Samples were synthesized, reduced, and characterized by C.T.P., V.A., Y.W., and M.R. under the supervision of D.G.S. and K.M.S. Electron microscopy was performed by B.H.G. under the supervision of L.F.K.. The manuscript was prepared by C.T.P. and K.M.S. with input from all authors.

DATA AVAILABILITY

The data that support the findings of this study are available within the paper and supplementary material. Additional data related to this study are available from the authors upon reasonable request.

-
- [1] D. Li, K. Lee, B. Y. Wang, M. Osada, S. Crossley, H. R. Lee, Y. Cui, Y. Hikita, and H. Y. Hwang, Superconductivity in an infinite-layer nickelate, *Nature* **572**, 624 (2019).
- [2] M. Osada, B. Y. Wang, B. H. Goodge, K. Lee, H. Yoon, K. Sakuma, D. Li, M. Miura, L. F. Kourkoutis, and H. Y. Hwang, A Superconducting Praseodymium Nickelate with Infinite Layer Structure, *Nano Letters* **20**, 5735 (2020).
- [3] M. Osada, B. Y. Wang, B. H. Goodge, S. P. Harvey, K. Lee, D. Li, L. F. Kourkoutis, and H. Y. Hwang, Nickelate Superconductivity without Rare-Earth Magnetism: (La,Sr)NiO₂, *Advanced Materials* **33**, 2104083 (2021).
- [4] S. Zeng, C. Li, L. E. Chow, Y. Cao, Z. Zhang, C. S. Tang, X. Yin, Z. S. Lim, J. Hu, P. Yang, and A. Ariando, Superconductivity in infinite-layer nickelate La_{1-x}Ca_xNiO₂ thin films, *Science Advances* **8**, eabl9927 (2022).
- [5] J. Zhang, H. Zheng, Y. Ren, and J. F. Mitchell, High-Pressure Floating-Zone Growth of Perovskite Nickelate LaNiO₃ Single Crystals, *Crystal Growth and Design* **17**, 2730 (2017).
- [6] H. Zheng, J. Zhang, B. Wang, D. Phelan, M. J. Krogstad, Y. Ren, W. A. Phelan, O. Chmaissem, B. Poudel, and J. F. Mitchell, High pO₂ Floating Zone Crystal Growth of the Perovskite Nickelate PrNiO₃, *Crystals* **9**, 324 (2019).
- [7] P. Puphal, Y.-M. Wu, K. Fürsich, H. Lee, M. Pakdaman, J. A. N. Bruin, J. Nuss, Y. E. Suyolcu, P. A. van Aken, B. Keimer, M. Isobe, and M. Hepting, Topotactic transformation of single crystals: From perovskite to infinite-layer nickelates, *Science Advances* **7**, eabl8091 (2021).
- [8] P. Puphal, V. Pomjakushin, R. A. Ortiz, S. Hammoud, M. Isobe, B. Keimer, and M. Hepting, Investigation of hydrogen incorporations in bulk infinite-layer nickelates, *Frontiers in Physics* **10**, 1 (2022).
- [9] M. Huo, Z. Liu, H. Sun, L. Li, H. Lui, C. Huang, F. Liang, B. Shen, and M. Wang, Synthesis and properties of La_{1-x}Sr_xNiO₃ and La_{1-x}Sr_xNiO₂, *Chinese Physics B* **31**, 107401 (2022).
- [10] P. Puphal, B. Wehinger, J. Nuss, K. Küster, U. Starke, G. Garbarino, B. Keimer, M. Isobe, and M. Hepting, Synthesis and physical properties of LaNiO₂ crystals, *Physical Review Materials* **7**, 014804 (2023).
- [11] Y.-m. Wu, P. Puphal, H. Lee, J. Nuss, M. Isobe, B. Keimer, M. Hepting, Y. E. Suyolcu, and P. A. van Aken, Topotactically induced oxygen vacancy order in nickelate single crystals, *Physical Review Materials* **7**, 053609 (2023).
- [12] C. Domínguez, A. B. Georgescu, B. Mundet, Y. Zhang, J. Fowlie, A. Mercy, A. Waelchli, S. Catalano, D. T. Alexander, P. Ghosez, A. Georges, A. J. Millis, M. Gibert, and J. M. Triscone, Length scales of interfacial coupling between metal and insulator phases in oxides, *Nature Materials* **19**, 1182 (2020).
- [13] Q. Song, S. Doyle, G. A. Pan, I. El Baggari, D. Ferenc Segedin, D. Córdova Carrizales, J. Nordlander, C. Tzschaschel, J. R. Ehrets, Z. Hasan, H. El-Sherif, J. Krishna, C. Hanson, H. LaBollita, A. Bostwick, C. Jozwiak, E. Rotenberg, S.-Y. Xu, A. Lanzara, A. T. N'Diaye, C. A. Heikes, Y. Liu, H. Paik, C. M. Brooks, B. Pamuk, J. T. Heron, P. Shafer, W. D. Ratcliff, A. S. Botana, L. Moreschini, and J. A. Mundy, Antiferromagnetic metal phase in an electron-doped rare-earth nickelate, *Nature Physics* **19**, 522 (2023).
- [14] C. Domínguez, J. Fowlie, A. B. Georgescu, B. Mundet, N. Jaouen, M. Viret, A. Suter, A. J. Millis, Z. Salman, T. Prokscha, M. Gibert, and J.-M. Triscone, Coupling of magnetic phases at nickelate interfaces, *Physical Review Materials* **7**, 065002 (2023).
- [15] E. Breckenfeld, Z. Chen, A. R. Damodaran, and L. W. Martin, Effects of nonequilibrium growth, nonstoichiometry, and film orientation on the metal-to-insulator transition in NdNiO₃ thin films, *ACS Applied Materials and Interfaces* **6**, 22436 (2014).
- [16] D. Preziosi, A. Sander, A. Barthélémy, and M. Bibes, Reproducibility and off-stoichiometry issues in nickelate thin films grown by pulsed laser deposition,

[AIP Advances 7, 015210 \(2017\)](#).

- [17] T. Yamanaka, A. N. Hattori, L. N. Pamasi, S. Takemoto, K. Hattori, H. Daimon, K. Sato, and H. Tanaka, Effects of Off-Stoichiometry in the Epitaxial NdNiO₃ Film on the Suppression of Its Metal-Insulator-Transition Properties, [ACS Applied Electronic Materials 1, 2678 \(2019\)](#).
- [18] Y. Li, W. Sun, J. Yang, X. Cai, W. Guo, Z. Gu, Y. Zhu, and Y. Nie, Impact of Cation Stoichiometry on the Crystalline Structure and Superconductivity in Nickelates, [Frontiers in Physics 9, 1 \(2021\)](#).
- [19] S. Heo, C. Oh, J. Son, and H. M. Jang, Influence of tensile-strain-induced oxygen deficiency on metal-insulator transitions in NdNiO_{3-δ} epitaxial thin films, [Scientific Reports 7, 1 \(2017\)](#).
- [20] A. J. Hauser, E. Mikheev, N. E. Moreno, J. Hwang, J. Y. Zhang, and S. Stemmer, Correlation between stoichiometry, strain, and metal-insulator transitions of NdNiO₃ films, [Applied Physics Letters 106, 092104 \(2015\)](#).
- [21] D. Ferenc Segedin, B. H. Goodge, G. A. Pan, Q. Song, H. LaBollita, M.-C. Jung, H. El-Sherif, S. Doyle, A. Turkiewicz, N. K. Taylor, J. A. Mason, A. T. N'Diaye, H. Paik, I. El Baggari, A. S. Botana, L. F. Kourkoutis, C. M. Brooks, and J. A. Mundy, Limits to the strain engineering of layered square-planar nickelate thin films, [Nature Communications 14, 1468 \(2023\)](#).
- [22] K. Lee, B. H. Goodge, D. Li, M. Osada, B. Y. Wang, Y. Cui, L. F. Kourkoutis, and H. Y. Hwang, Aspects of the synthesis of thin film superconducting infinite-layer nickelates, [APL Materials 8, 041107 \(2020\)](#).
- [23] M. A. Hayward, M. A. Green, M. J. Rosseinsky, and J. Sloan, Sodium Hydride as a Powerful Reducing Agent for Topotactic Oxide Deintercalation: Synthesis and Characterization of the Nickel(I) Oxide LaNiO₂, [Journal of the American Chemical Society 121, 8843 \(1999\)](#).
- [24] M. Hayward and M. Rosseinsky, Synthesis of the infinite layer Ni(I) phase NdNiO_{2+x} by low temperature reduction of NdNiO₃ with sodium hydride, [Solid State Sciences 5, 839 \(2003\)](#).
- [25] K. G. Tschersich and V. von Bonin, Formation of an atomic hydrogen beam by a hot capillary, [Journal of Applied Physics 84, 4065 \(1998\)](#).
- [26] K. G. Tschersich, J. P. Fleischhauer, and H. Schuler, Design and characterization of a thermal hydrogen atom source, [Journal of Applied Physics 104, 034908 \(2008\)](#).
- [27] P.-H. Xiang, N. Zhong, C.-G. Duan, X. D. Tang, Z. G. Hu, P. X. Yang, Z. Q. Zhu, and J. H. Chu, Strain controlled metal-insulator transition in epitaxial NdNiO₃ thin films, [Journal of Applied Physics 114, 243713 \(2013\)](#).
- [28] P. D. C. King, H. I. Wei, Y. F. Nie, M. Uchida, C. Adamo, S. Zhu, X. He, I. Božović, D. G. Schlom, and K. M. Shen, Atomic-scale control of competing electronic phases in ultrathin LaNiO₃, [Nature Nanotechnology 9, 443 \(2014\)](#).
- [29] J. Sun, C. T. Parzyck, J. H. Lee, C. M. Brooks, L. F. Kourkoutis, X. Ke, R. Misra, J. Schubert, F. V. Hensling, M. R. Barone, Z. Wang, M. E. Holtz, N. J. Schreiber, Q. Song, H. Paik, T. Heeg, D. A. Muller, K. M. Shen, and D. G. Schlom, Canonical approach to cation flux calibration in oxide molecular-beam epitaxy, [Physical Review Materials 6, 033802 \(2022\)](#).
- [30] J. B. Nelson and D. P. Riley, An experimental investigation of extrapolation methods in the derivation of accurate unit-cell dimensions of crystals, [Proceedings of the Physical Society 57, 160 \(1945\)](#).
- [31] G. A. Pan, Q. Song, D. Ferenc Segedin, M. C. Jung, H. El-Sherif, E. E. Fleck, B. H. Goodge, S. Doyle, D. Córdoba Carrizales, A. T. N'Diaye, P. Shafer, H. Paik, L. F. Kourkoutis, I. El Baggari, A. S. Botana, C. M. Brooks, and J. A. Mundy, Synthesis and electronic properties of Nd_{n+1}Ni_nO_{3n+1} Ruddlesden-Popper nickelate thin films, [Physical Review Materials 6, 055003 \(2022\)](#).
- [32] Y. M. Klein, M. Kozłowski, A. Linden, P. Lacorre, M. Medarde, and D. J. Gawryluk, RENiO₃ Single Crystals (RE = Nd, Sm, Gd, Dy, Y, Ho, Er, Lu) Grown from Molten Salts under 2000 bar of Oxygen Gas Pressure, [Crystal Growth & Design 21, 4230 \(2021\)](#).
- [33] M. D. Biegalski, D. D. Fong, J. A. Eastman, P. H. Fuoss, S. K. Streiffer, T. Heeg, J. Schubert, W. Tian, C. T. Nelson, X. Q. Pan, M. E. Hawley, M. Bernhagen, P. Reiche, R. Uecker, S. Trolier-McKinstry, and D. G. Schlom, Critical thickness of high structural quality SrTiO₃ films grown on orthorhombic (101) DyScO₃, [Journal of Applied Physics 104, 114109 \(2008\)](#).
- [34] B. H. Goodge, I. El Baggari, S. S. Hong, Z. Wang, D. G. Schlom, H. Y. Hwang, and L. F. Kourkoutis, Disentangling Coexisting Structural Order Through Phase Lock-In Analysis of Atomic-Resolution STEM Data, [Microscopy and Microanalysis 28, 404 \(2022\)](#).
- [35] M. Crespin, B. Y. P. Levitz, and L. Gataineau, Reduced Forms of LaNiO₃ Perovskite, [J. Chem. Soc., Faraday Transactions II 79, 1181 \(1983\)](#).
- [36] M. Crespin, O. Isnard, F. Dubois, J. Choisnet, and P. Odier, LaNiO₂: Synthesis and structural characterization, [Journal of Solid State Chemistry 178, 1326 \(2005\)](#).
- [37] M. Kawai, S. Inoue, M. Mizumaki, N. Kawamura, N. Ichikawa, and Y. Shimakawa, Reversible changes of epitaxial thin films from perovskite LaNiO₃ to infinite-layer structure LaNiO₂, [Applied Physics Letters 94, 082102 \(2009\)](#).
- [38] A. Ikeda, Y. Krockenberger, H. Irie, M. Naito, and H. Yamamoto, Direct observation of infinite NiO₂ planes in LaNiO₂ films, [Appl. Phys. Express 9, 061101 \(2016\)](#).
- [39] T. Onozuka, A. Chikamatsu, T. Katayama, T. Fukumura, and T. Hasegawa, Formation of defect-fluorite structured NdNiO_xH_y epitaxial thin films via a soft chemical route from NdNiO₃ precursors, [Dalton Transactions 45, 12114 \(2016\)](#).
- [40] D. Li, B. Y. Wang, K. Lee, S. P. Harvey, M. Osada, B. H. Goodge, L. F. Kourkoutis, and H. Y. Hwang, Superconducting Dome in Nd_{1-x}Sr_xNiO₂ Infinite Layer Films, [Physical Review Letters 125, 027001 \(2020\)](#).
- [41] S. Zeng, C. S. Tang, X. Yin, C. Li, M. Li, Z. Huang, J. Hu, W. Liu, G. J. Omar, H. Jani, Z. S. Lim, K. Han, D. Wan, P. Yang, S. J. Pennycook, A. T. S. Wee, and A. Ariando, Phase Diagram and Superconducting Dome of Infinite-Layer Nd_{1-x}Sr_xNiO₂ Thin Films, [Physical Review Letters 125, 147003 \(2020\)](#).
- [42] M. Osada, B. Y. Wang, K. Lee, D. Li, and H. Y. Hwang, Phase diagram of infinite layer praseodymium nickelate pr_{1-x}sr_xnio₂ thin films, [Phys. Rev. Mater. 4, 121801 \(2020\)](#).
- [43] G. Krieger, A. Raji, L. Schlur, G. Versini, C. Bouillet, M. Lenertz, J. Robert, A. Gloter, N. Viart, and D. Preziosi, Synthesis of infinite-layer nickelates and influence of the capping-layer on magnetotransport, [Journal of Physics D: Applied Physics 56, 024003 \(2023\)](#).
- [44] A. Ikeda, T. Manabe, and M. Naito, Comparison of reduction agents in the synthesis of infinite-layer LaNiO₂ films, [Physica C: Superconductivity and its Applications 506, 83 \(2014\)](#).
- [45] Q. Gao, Y. Zhao, X.-J. Zhou, and Z. Zhu, Preparation of Superconducting Thin Films of Infinite-Layer Nickelate Nd_{0.8}Sr_{0.2}NiO₂, [Chinese Physics Letters 38, 077401 \(2021\)](#).
- [46] Q. Gu, Y. Li, S. Wan, H. Li, W. Guo, H. Yang, Q. Li, X. Zhu, X. Pan, Y. Nie, and H. H. Wen, Single particle tunneling spectrum of superconducting Nd_{1-x}Sr_xNiO₂ thin films,

Nature Communications **11**, 1 (2020).

- [47] Z. Chen, M. Osada, D. Li, E. M. Been, S. D. Chen, M. Hashimoto, D. Lu, S. K. Mo, K. Lee, B. Y. Wang, F. Rodolakis, J. L. McChesney, C. Jia, B. Moritz, T. P. Devereaux, H. Y. Hwang, and Z. X. Shen, Electronic structure of superconducting nickelates probed by resonant photoemission spectroscopy, *Matter* **5**, 1806 (2022).
- [48] R.-F. Wang, Y.-L. Xiong, H. Yan, X. Hu, M. Osada, D. Li, H. Y. Hwang, C.-L. Song, X.-C. Ma, and Q.-K. Xue, Observation of Coulomb blockade and Coulomb staircases in superconducting $\text{Pr}_{0.8}\text{Sr}_{0.2}\text{NiO}_2$ films, *Physical Review B* **107**, 115411 (2023).
- [49] W. Wei, K. Shin, H. Hong, Y. Shin, A. S. Thind, Y. Yang, R. F. Klie, F. J. Walker, and C. H. Ahn, Solid state reduction of nickelate thin films, *Physical Review Materials* **7**, 013802 (2023).
- [50] W. Wei, D. Vu, Z. Zhang, F. J. Walker, and C. H. Ahn, Superconducting $\text{Nd}_{1-x}\text{Eu}_x\text{NiO}_2$ thin films using in situ synthesis, *Science Advances* **9**, eadh3327 (2023).
- [51] A. A. Bergh, Atomic Hydrogen as a Reducing Agent, *Bell System Technical Journal* **44**, 261 (1965).
- [52] S. M. Gates, R. R. Kunz, and C. Greenlief, Silicon hydride etch products from the reaction of atomic hydrogen with Si(100), *Surface Science* **207**, 364 (1989).
- [53] G. Bell, N. Kaijaks, R. Dixon, and C. McConville, Atomic hydrogen cleaning of polar III-V semiconductor surfaces, *Surface Science* **401**, 125 (1998).
- [54] I. Nishiyama, H. Oizumi, K. Motai, A. Izumi, T. Ueno, H. Akiyama, and A. Namiki, Reduction of oxide layer on Ru surface by atomic-hydrogen treatment, *JVST B: Microelectronics and Nanometer Structures* **23**, 3129 (2005).
- [55] W. Huang, W. Ranke, and R. Schlögl, Reduction of an $\alpha\text{-Fe}_2\text{O}_3(0001)$ film using atomic hydrogen, *Journal of Physical Chemistry C* **111**, 2198 (2007).
- [56] J. Knudsen, L. R. Merte, L. C. Grabow, F. M. Eichhorn, S. Porsgaard, H. Zeuthen, R. T. Vang, E. Lægsgaard, M. Mavrikakis, and F. Besenbacher, Reduction of FeO/Pt(111) thin films by exposure to atomic hydrogen, *Surface Science* **604**, 11 (2010).
- [57] S. M. F. Shahed, T. Hasegawa, Y. Sainoo, Y. Watanabe, N. Isomura, A. Beniya, H. Hirata, and T. Komeda, STM and XPS study of $\text{CeO}_2(111)$ reduction by atomic hydrogen, *Surface Science* **628**, 30 (2014).
- [58] K. Takahashi, D. Matthey, D. Jaccard, and J.-M. Triscone, Transport properties of reduced SrTiO_3 single crystal “thin films”, *Annalen der Physik* **13**, 68 (2004).
- [59] Z. Meng, H. Yan, P. Qin, X. Zhou, X. Wang, H. Chen, L. Liu, and Z. Liu, Topotactic Transition: A Promising Opportunity for Creating New Oxides, *Advanced Functional Materials*, 1 (2023).
- [60] W. Zheng and A. Gallagher, Hydrogen dissociation on high-temperature tungsten, *Surface Science* **600**, 2207 (2006).
- [61] J. M. González-Calbet, M. J. Sayagués, and M. Vallet-Regí, An electron diffraction study of new phases in the LaNiO_{3-x} system, *Solid State Ionics* **32-33**, 721 (1989).
- [62] T. Moriga, O. Usaka, I. Nakabayashi, Y. Hirashima, T. Kohno, S. Kikkawa, and F. Kanamaru, Reduction of the perovskite-type LnNiO_3 ($\text{Ln}=\text{Pr},\text{Nd}$) to $\text{Ln}_3\text{Ni}_3\text{O}_7$ with monovalent nickel ions, *Solid State Ionics* **74**, 211 (1994).
- [63] M. Sayagués, M. Vallet-Regí, A. Caneiro, and J. González-Calbet, Microstructural Characterization of the LaNiO_{3-y} System, *Journal of Solid State Chemistry* **110**, 295 (1994).
- [64] J. A. Alonso and M. J. Martínez-Lope, Preparation and crystal structure of the deficient perovskite $\text{LaNiO}_{2.5}$, solved from neutron powder diffraction data, *Journal of the Chemical Society, Dalton Transactions*, 2819 (1995).
- [65] T. Moriga, M. Hayashi, T. Sakamoto, M. Orihara, and I. Nakabayashi, Reduction processes of rare-earth nickelate perovskites LnNiO_3 ($\text{Ln}=\text{La}, \text{Pr}, \text{Nd}$), *Solid State Ionics* **154-155**, 251 (2002).
- [66] B.-X. Wang, H. Zheng, E. Kriviyakina, O. Chmaissem, P. P. Lopes, J. W. Lynn, L. C. Gallington, Y. Ren, S. Rosenkranz, J. F. Mitchell, and D. Phelan, Synthesis and characterization of bulk $\text{Nd}_{1-x}\text{Sr}_x\text{NiO}_2$ and $\text{Nd}_{1-x}\text{Sr}_x\text{NiO}_3$, *Physical Review Materials* **4**, 084409 (2020).
- [67] A. Raji, G. Krieger, N. Viart, D. Preziosi, J.-P. Rueff, and A. Gloter, Charge distribution across capped and uncapped infinite-layer neodymium nickelate thin films, *Small* **19**, 2304872 (2023).
- [68] C. T. Parzyck, N. K. Gupta, Y. Wu, V. Anil, L. Bhatt, M. Bouliane, R. Gong, B. Z. Gregory, A. Luo, R. Sutarto, F. He, Y. D. Chuang, T. Zhou, G. Herranz, L. F. Kourkoutis, A. Singer, D. G. Schlom, D. G. Hawthorn, and K. M. Shen, Absence of $3a_0$ charge density wave order in the infinite layer nickelates (2023), [arXiv:2307.06486 \[cond-mat.supr-con\]](https://arxiv.org/abs/2307.06486).
- [69] D. Krieger, E. Wintersberger, and J. Stangl, xrayutilities : a versatile tool for reciprocal space conversion of scattering data recorded with linear and area detectors, *Journal of Applied Crystallography* **46**, 1162 (2013).
- [70] B. H. Goodge, B. Geisler, K. Lee, M. Osada, B. Y. Wang, D. Li, H. Y. Hwang, R. Pentcheva, and L. F. Kourkoutis, Resolving the polar interface of infinite-layer nickelate thin films, *Nature Materials* **22**, 466 (2023), 2201.03613.
- [71] K. Lee, B. Y. Wang, M. Osada, B. H. Goodge, T. C. Wang, Y. Lee, S. Harvey, W. J. Kim, Y. Yu, C. Murthy, S. Raghu, L. F. Kourkoutis, and H. Y. Hwang, Linear-in-temperature resistivity for optimally superconducting $(\text{Nd},\text{Sr})\text{NiO}_2$, *Nature* **619**, 288 (2023).
- [72] Y. Kobayashi, Z. Li, K. Hirai, C. Tassel, F. Loyer, N. Ichikawa, N. Abe, T. Yamamoto, Y. Shimakawa, K. Yoshimura, M. Takano, O. J. Hernandez, and H. Kageyama, Gas phase contributions to topochemical hydride reduction reactions, *Journal of Solid State Chemistry* **207**, 190 (2013).
- [73] G. Krieger, L. Martinelli, S. Zeng, L. E. Chow, K. Kummer, R. Arpaia, M. Moretti Sala, N. B. Brookes, A. Ariando, N. Viart, M. Salluzzo, G. Ghiringhelli, and D. Preziosi, Charge and Spin Order Dichotomy in NdNiO_2 Driven by the Capping Layer, *Physical Review Letters* **129**, 027002 (2022).
- [74] G. A. Pan, D. Ferenc Segedin, H. LaBollita, Q. Song, E. M. Nica, B. H. Goodge, A. T. Pierce, S. Doyle, S. Novakov, D. Córdoba Carrizales, A. T. N’Diaye, P. Shafer, H. Paik, J. T. Heron, J. A. Mason, A. Yacoby, L. F. Kourkoutis, O. Erten, C. M. Brooks, A. S. Botana, and J. A. Mundy, Superconductivity in a quintuple-layer square-planar nickelate, *Nature Materials* **21**, 160 (2022).
- [75] W. J. Kim, M. A. Smeaton, C. Jia, B. H. Goodge, B.-G. Cho, K. Lee, M. Osada, D. Jost, A. V. Ievlev, B. Moritz, L. F. Kourkoutis, T. P. Devereaux, and H. Y. Hwang, Geometric frustration of Jahn–Teller order in the infinite-layer lattice, *Nature* **615**, 237 (2023).
- [76] Y. Tsujimoto, C. Tassel, N. Hayashi, T. Watanabe, H. Kageyama, K. Yoshimura, M. Takano, M. Ceretti, C. Ritter, and W. Paulus, Infinite-layer iron oxide with a square-planar coordination, *Nature* **450**, 1062 (2007).
- [77] S. Inoue, M. Kawai, Y. Shimakawa, M. Mizumaki, N. Kawamura, T. Watanabe, Y. Tsujimoto, H. Kageyama, and K. Yoshimura, Single-crystal epitaxial thin films of SrFeO_2 with FeO_2 “infinite layers”, *Applied Physics Letters* **92**, 161911 (2008).

- [78] J. Hadermann, A. M. Abakumov, J. J. Adkin, and M. A. Hayward, Topotactic Reduction As a Route to New Close-Packed Anion Deficient Perovskites: Structure and Magnetism of 4H-BaMnO_{2+x} , *Journal of the American Chemical Society* **131**, 10598 (2009).
- [79] K. Matsumoto, M. Haruta, M. Kawai, A. Sakaiguchi, N. Ichikawa, H. Kurata, and Y. Shimakawa, Artificial Superlattice Thin Film of Infinite-Layer Structure $[\text{CaFeO}_2]/[\text{SrFeO}_2]$, *Applied Physics Express* **3**, 105601 (2010).
- [80] E. J. Moon, Y. Xie, E. D. Laird, D. J. Keavney, C. Y. Li, and S. J. May, Fluorination of Epitaxial Oxides: Synthesis of Perovskite Oxyfluoride Thin Films, *Journal of the American Chemical Society* **136**, 2224 (2014).
- [81] T. Mairoser, J. A. Mundy, A. Melville, D. Hodash, P. Cueva, R. Held, A. Glavic, J. Schubert, D. A. Muller, D. G. Schlom, and A. Schmehl, High-quality EuO thin films the easy way via topotactic transformation, *Nature Communications* **6**, 7716 (2015).
- [82] G. Koster, B. L. Kropman, G. J. H. M. Rijnders, D. H. A. Blank, and H. Rogalla, Quasi-ideal strontium titanate crystal surfaces through formation of strontium hydroxide, *Applied Physics Letters* **73**, 2920 (1998).
- [83] I. Miccoli, F. Edler, H. Pfnür, and C. Tegenkamp, The 100th anniversary of the four-point probe technique: The role of probe geometries in isotropic and anisotropic systems, *Journal of Physics Condensed Matter* **27**, 223201 (2015).
- [84] B. H. Savitzky, I. El Baggari, C. B. Clement, E. Waite, B. H. Goodge, D. J. Baek, J. P. Sheckelton, C. Pasco, H. Nair, N. J. Schreiber, J. Hoffman, A. S. Admasu, J. Kim, S.-W. Cheong, A. Bhattacharya, D. G. Schlom, T. M. McQueen, R. Hovden, and L. F. Kourkoutis, Image registration of low signal-to-noise cryo-STEM data, *Ultramicroscopy* **191**, 56 (2018).

Supplemental Materials for: Synthesis of thin film infinite-layer nickelates by atomic hydrogen reduction: clarifying the role of the capping layer

C. T. Parzyck,¹ V. Anil,¹ Y. Wu,¹ B. H. Goodge,^{2,3} M. Roddy,¹
L. F. Kourkoutis,^{2,3} D. G. Schlom,^{3,4,5} and K. M. Shen^{1,3,6}

¹Laboratory of Atomic and Solid State Physics, Department of Physics, Cornell University, Ithaca, NY 14853, USA

²School of Applied and Engineering Physics, Cornell University, Ithaca, NY 14853, USA

³Kavli Institute at Cornell for Nanoscale Science, Cornell University, Ithaca, NY 14853, USA

⁴Department of Materials Science and Engineering, Cornell University, Ithaca, NY 14853, USA

⁵Leibniz-Institut für Kristallzüchtung, Max-Born-Straße 2, 12489 Berlin, Germany

⁶Institut de Ciència de Materials de Barcelona (ICMAB-CSIC), Campus UAB Bellaterra 08193, Spain

(Dated: January 17, 2024)

CONTENTS

I. Perovskite Nickelates	2
A. RHEED Oscillation Calibration	2
B. XRD and XRR Calibration	3
C. Effects of Non-Stoichiometry on Transport	4
D. Additional Aging Effect Data	4
II. Infinite-Layer Nickelates	7
A. AFM and XRD of Optimized Films	7
B. Reduction Effects on the Film Surface	8
References	11

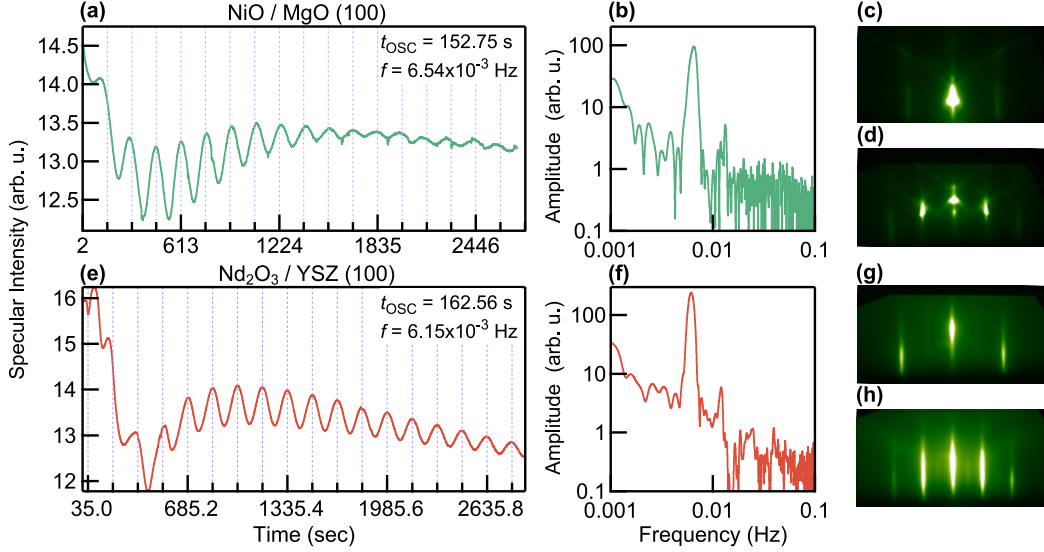


FIG. S1. RHEED Oscillations of the binary oxides NiO/MgO (100) and $\text{Nd}_2\text{O}_3/\text{YSZ}$ (111) used for calibration. (a) RHEED specular intensity of a NiO film during growth. (B) Fourier transform of the specular intensity showing a sharp peak at the monolayer frequency. (c-d) Post-growth RHEED images of the NiO film. (e-h) Same for a representative Nd_2O_3 film.

I. PEROVSKITE NICKELATES

The stoichiometric calibration of nickelate films is of paramount importance to the growth of high-quality NdNiO_3 . As the binary oxide constituents, Nd_2O_3 and NiO have negligible volatility, an absorption-controlled approach in molecular beam epitaxy (MBE) is not possible – excess deposited material either incorporates or forms precipitates – both of which negatively impact the film quality. Studies of the pulsed laser deposition (PLD) and MBE growth of nickelates indicate that deviation from a cation ratio of 1:1 has strong effects on the electrical properties of NdNiO_3 films [1–4] and a strong influence on the quality of subsequently reduced films – particularly the presence of Ruddlesden-Popper (RP) intergrowths [5–7]. In PLD growth, careful control of the film stoichiometry can be achieved through control of the laser fluence and source material (by repolishing the target surface to combat laser-induced changes [2], for instance). In MBE, on the other hand, the key is to establish the elemental source fluxes with a high degree of accuracy. We find that the typical accuracy of a quartz crystal microbalance (QCM), 10-15%, is not sufficient to reproducibly grow high-quality nickelate films; we follow instead a two-step calibration procedure detailed here.

A. RHEED Oscillation Calibration

Initial flux measurements are obtained by monitoring RHEED oscillations during the growths of Nd_2O_3 on $(\text{ZrO}_2)_{0.905}(\text{Y}_2\text{O}_3)_{0.095}$ (111) and NiO on MgO (100) using the parameters outlined in Sun et al. [8]. In Fig. S1 we detail the RHEED oscillation measurements of NiO and Nd_2O_3 in (a-d) and (e-h), respectively. While both compounds grow over a very wide range of conditions (ozone flux, substrate temperature) we find the optimal conditions for RHEED oscillations of NiO are around 450 °C (following an 800 °C vacuum anneal to clean the MgO surface). Conversely, it is preferable to grow Nd_2O_3 at higher temperatures, ~ 970 °C to stabilize the hexagonal structure; though often the first few layers will take on a bixbyite structure, evidenced by a noticeably different oscillation frequency as seen in (e). By monitoring the RHEED specular intensity in (a) and (e) and performing a Fourier transform, (b) and (f), the monolayer formation time can be easily extracted and converted into an elemental flux.

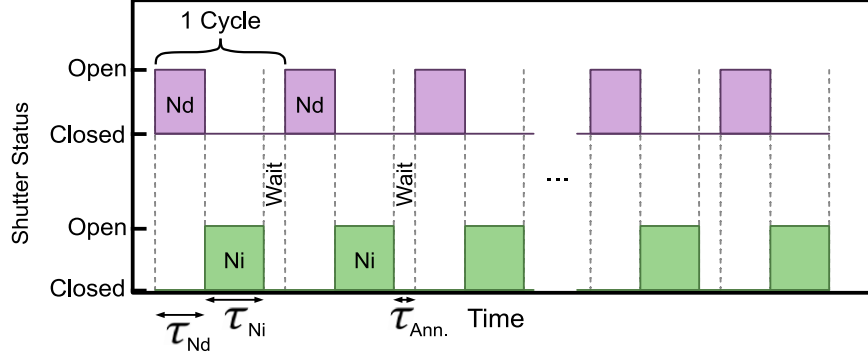


FIG. S2. Shutter timing diagram illustrating the sequential deposition of NdNiO₃ thin films. The shutters for the neodymium and nickel sources are opened in sequence for time periods τ_{Nd} and τ_{Ni} , respectively. Between each cycle the sample is ozone annealed with the shutters closed for a short period of $\tau_{\text{Ann.}} = 5$ seconds to promote full oxidation of the nickel layer, as in Ref. [9].

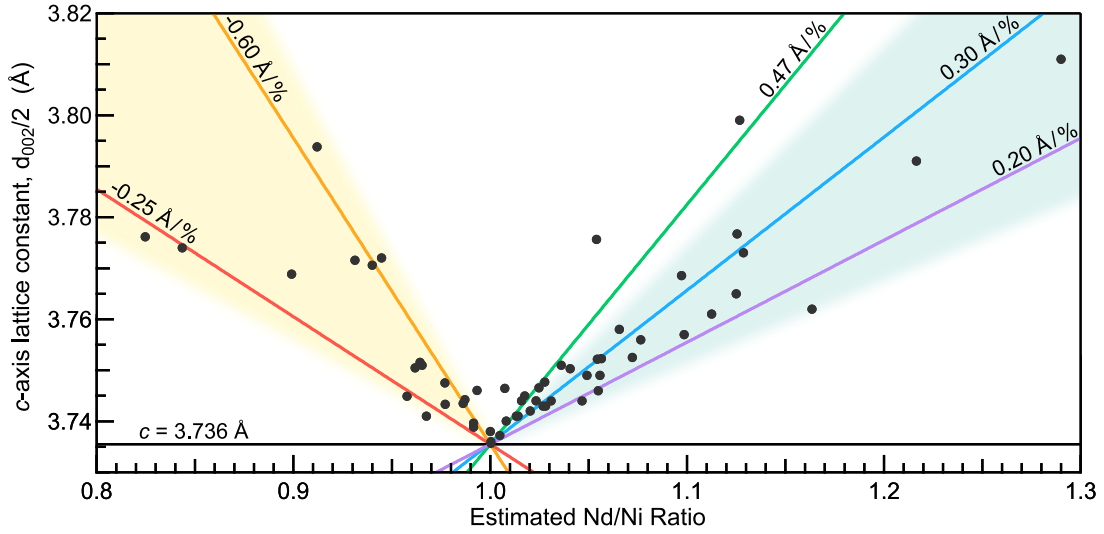


FIG. S3. X-ray diffraction calibration data for 20 u.c. thick films of NdNiO₃ on (001) SrTiO₃. c -axis lattice constant, determined from the 002 peak position, as a function of the nominal cation ratio Nd:Ni. Slopes of typical correction factors employed in the optimization procedure are labeled.

B. XRD and XRR Calibration

While the aforementioned calibration method greatly improves upon the basic calibration using a QCM, we find that its accuracy is typically limited to the few percent scale for each source and as such requires further refinement. This is accomplished using the method described by Li et al. in Ref. 6: the c -axis lattice constant (in our case the 002 peak position) is used as a proxy for non-stoichiometry with the minimal value of the lattice constant corresponding to a stoichiometric cation ratio of Nd:Ni = 1:1. Our repetition of this procedure produces much the same qualitative characteristics as in Ref. [6], although with a slightly lower minimal lattice constant of $c = 3.736$ Å, and is detailed in Fig. S3. To construct this diagram we start by growing a sequence of films with differing shutter times, $\tau_{\text{Nd,Ni}}$, and record the ratio $\tau_{\text{Nd}}/\tau_{\text{Ni}}$. The shutter times τ_{Nd} and τ_{Ni} correspond to our best estimate of the time to deposit a single monolayer of NdO and NiO₂, respectively. A timing diagram showing the sequential opening of the Nd and Ni shutters in a constant background partial pressure of O₃ with a short, 5 second, anneal between cycles is provided in Fig. S2. While the flux ratio $\Phi_{\text{Nd}}/\Phi_{\text{Ni}}$ is not known *a priori*, once the growth sequence converges to near the minimal value this ratio can be calculated from

$$1 = \frac{\Phi_{\text{Nd}}}{\Phi_{\text{Ni}}} \times \frac{\tau_{\text{Nd,f}}}{\tau_{\text{Ni,f}}}$$

and applied to the whole sequence to determine the Nd:Ni ratio for all films. Figure S3 is an aggregation of many such growth runs. The scatter increases as we depart from Nd:Ni = 1:1, which is a consequence of source drift on the above procedure. Though modern effusion cells provide excellent flux stability, often reducing flux drift to less than 1% per hour, the difference between $\tau_{\text{Nd}}/\tau_{\text{Ni}}$ at the start of the run and the end (when 1:1 is reached) means that estimation of Nd:Ni for the first samples in the sequence (Nd:Ni \gg 1) is less accurate than at the end (Nd:Ni \sim 1). This estimated cone of uncertainty is illustrated by the shaded regions. Despite this uncertainty in the non-stoichiometry of films well away from 1:1, in the region near the minimum lattice constant discernible changes are still observed down to single percent changes in the shutter times, evidencing that this method can be used to hone the non-stoichiometry down to the percent level or less.

A typical optimization routine at the start of a growth campaign consists of starting with the RHEED oscillation calibration of one or both of Nd and Ni. Then the starting shutter times are calculated to begin with a few percent of excess Neodymium to bias the initial growth towards Nd:Ni $>$ 1; this is to ensure that the direction of the first step is known *a priori* (i.e., reducing the Nd shutter time) and to avoid venturing into the Ni-rich side of the diagram. We find that on the Ni-rich side the relationship between d_{002} and the shutter times is less repeatable. We attribute this to the propensity of excess Ni to precipitate out of the film in the form of NiO, rather than readily incorporating like neodymium does. The flux ratio can then be ‘walked-in’ to 1:1 by progressive adjustment of the shutter times, growth, and XRD measurement. If the starting Nd excess is greater than 10% or so an ‘aggressive’ adjustment factor of 0.2 to 0.3 Å/% can be used in tuning the shutter times between subsequent films; as Nd excess is further reduced more conservative values of 0.3 to 0.47 Å/% are used to avoid accidentally jumping over onto the Ni-rich side. Once the Nd:Ni ratio is within 5-7% of the 1:1 stoichiometric ratio, the total film thickness can also be fine-tuned (by changing τ_{Nd} and τ_{Ni} by the same fraction) to match the desired number of unit cells, typically 20, based on x-ray reflectivity (XRR) measurements of the NdNiO₃ film thickness.

C. Effects of Non-Stoichiometry on Transport

Here we describe the effects of non-stoichiometry on the transport properties of NdNiO₃ films grown on (001) SrTiO₃. The temperature dependent resistivity of a sequence of samples of varying lattice constants (and estimated non-stoichiometry based on Fig. S3) are presented in Fig. S4. The film with the lowest lattice constant has a low room-temperature resistivity of $\sim 200\mu\Omega\text{-cm}$, and a sharp metal-to-insulator transition (MIT) with a jump of nearly two decades. The structural quality is also evident in the accompanying RHEED image, where sharp diffraction peaks are visible on the primary and half-order streaks. As the Nd:Ni ratio is increased a clear increase in the resistivity is visible (up to an order of magnitude), along with a broadening of the MIT and widening of the hysteresis loop. At the same time the sharp diffraction peaks fade and the RHEED streaks become ‘peanut shaped’ – likely due to an increase in the film roughness. We note a marked difference between Nd-rich films under tensile strain when compared to prior measurements under compressive strain [1, 2] where excess Nd drives the films metallic. As previously noted in studies of non-stoichiometry on SrTiO₃ [3] the MIT temperature *increases* with increasing Nd content, and the MIT is not suppressed even up to very high levels (Nd:Ni \sim 1.25). Finally, on the nickel-rich side of the diagram broadening of the MIT and an overall increase of the resistivity are observed. These results indicate that a stoichiometric film on SrTiO₃ is the one with a minimum lattice constant, maximum transition sharpness, and minimum resistivity of the metallic state.

D. Additional Aging Effect Data

In Fig. S5 (unshifted) raw data corresponding to the sample aging study presented in Fig. 2 of the main text. Figs. S5(a) and S5(b) are reproduced from the main text for reference and Figs. S5(c) and S5(d) show data for the sample that was measured at much shorter intervals following growth. It is evident that in both cases a gradual increase of the film resistivity is present over time, with the room temperature values increasing by a factor of 4-5 over the course of ~ 3.5 weeks while stored in a dry, N₂ purged desiccator.

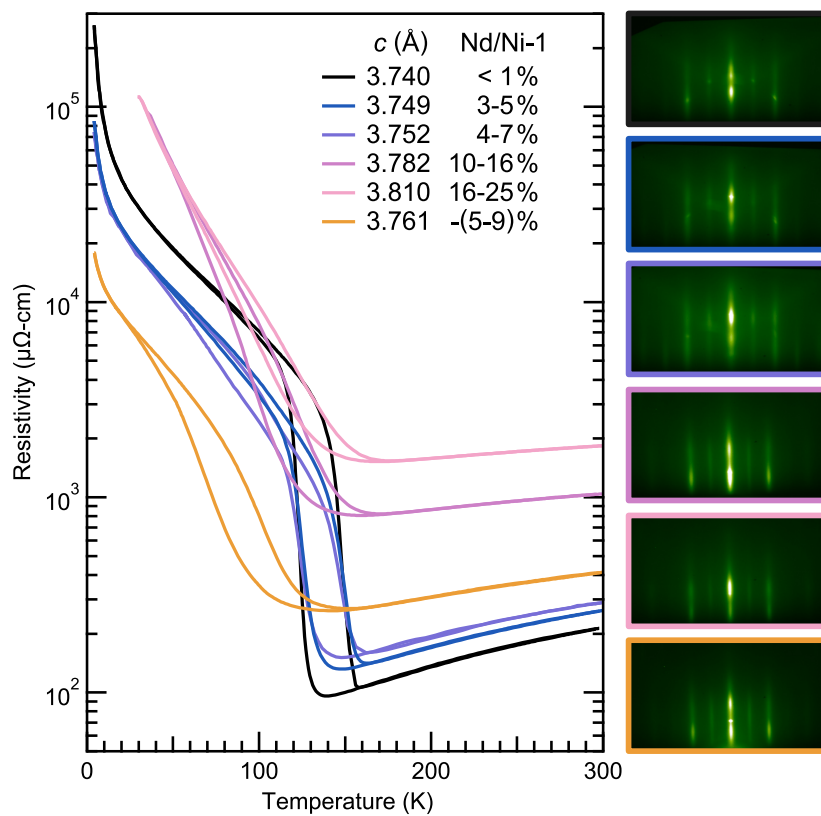


FIG. S4. Effects of cation non-stoichiometry on 20 u.c. thick NdNiO_3 thin films grown on (001)-oriented SrTiO_3 . Resistivity measurements of films of varying non-stoichiometry from slightly nickel rich to highly neodymium rich. Post-growth RHEED images, viewed along the $[110]_{\text{pc}}$ azimuth, of each of the films are pictured on the right. All images use a linear intensity scale.

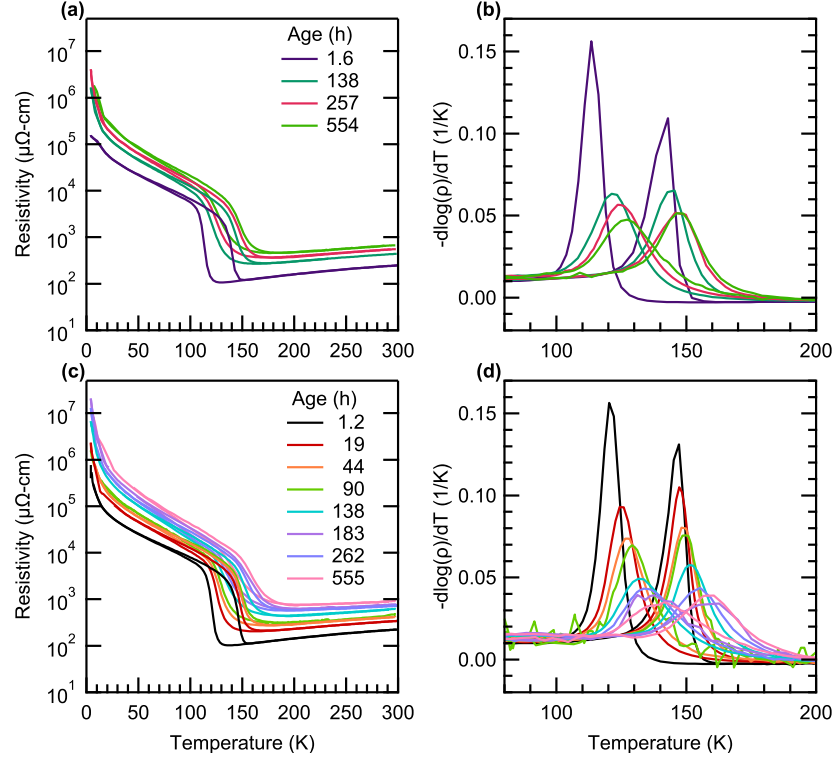


FIG. S5. Aging effects on the transport properties of stoichiometric NdNiO₃ films grown on SrTiO₃. (a) Resistivity of a single NdNiO₃ film measured periodically following growth, reproduced from the main text. (b) Logarithmic derivative of the transport curves in panel (a). (c) Resistivity of another film measured at a higher frequency over the same period of time as the one pictured in panel (a). (d) Logarithmic derivative of the resistivity curves in (c).

II. INFINITE-LAYER NICKELATES

A. AFM and XRD of Optimized Films

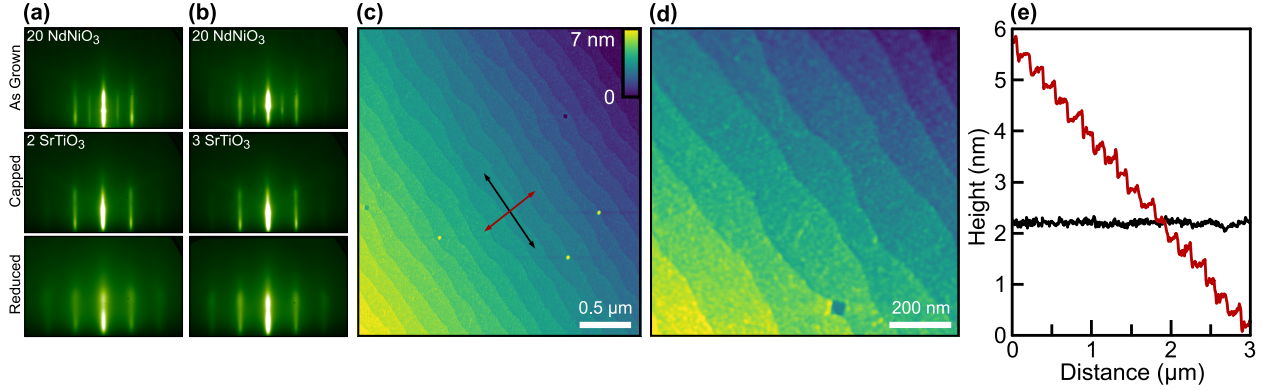


FIG. S6. Measurements of the surface quality of NdNiO_2 films reduced using atomic hydrogen. (a) RHEED images taken along the $[110]_{pc}$ azimuth of an as grown 20 u.c. thick NdNiO_3 film, the same film after capping with 2 u.c. of SrTiO_3 , and after atomic hydrogen reduction. (b) The same as in (a) but with a 3 u.c. thick SrTiO_3 cap. (c) AFM image of a 20 u.c. thick NdNiO_2 film capped with 2 u.c. of SrTiO_3 and reduced with atomic hydrogen; the extracted terrace-averaged RMS roughness is 124 ± 10 pm. (d) Zoom in on the stepped terraces. (e) Line profiles along (black) and across (red) the terraces showing preservation of the substrate's atomic steps. RHEED images in (a) and (b) use a linear intensity scale.

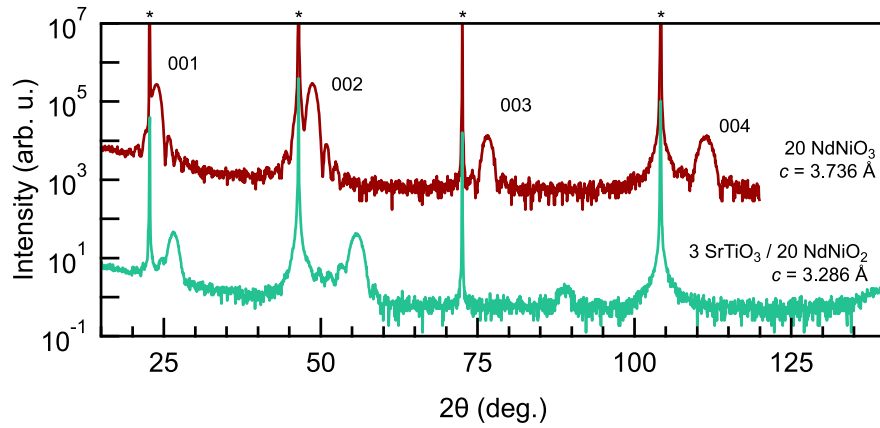


FIG. S7. Diffraction intensity along the specular direction for an uncapped 20 u.c. thick NdNiO_3 film and a 3 u.c. SrTiO_3 capped NdNiO_2 film grown on SrTiO_3 showing the $00L$ reflections. Nelson-Riley analysis of the infinite-layer film peaks gives a lattice constant of $c = 3.286$ Å. (*) indicates reflections from the (001) SrTiO_3 substrate.

In this section we present additional measurements of optimized, reduced NdNiO_2 films on SrTiO_3 . In Fig. S6 we show RHEED images and AFM topography of a reduced infinite-layer films. Figs. S6(a) and S6(b) present RHEED images of additional 20 u.c. thick NdNiO_3 films after growth, after capping, and after atomic hydrogen reduction. In both reduced films, reduced using the optimized three-step procedure, the preservation of the RHEED streaks indicates the film surface remains ordered. The RHEED images of both films are qualitatively similar, though the 3 u.c. capped film appears to have a slightly lower incoherent background than that of the film with the thinner cap. Figures S6(c)-(e) show AFM measurements of a 20 u.c. thick NdNiO_2 film capped with 2 u.c. of SrTiO_3 and reduced with atomic hydrogen. The reduced film shows a stepped terrace structure analogous to the atomically flat substrate on which it was grown, with a low surface roughness of ~ 124 pm. This is similar to films reduced using the solid-state aluminum reduction process introduced in Ref. 10. In Fig. S7 we show larger area $\theta - 2\theta$ scans of a perovskite, NdNiO_3 , film and an optimized, reduced infinite-layer, NdNiO_2 , film which cover all of the $00L$ peaks observable

with Cu $K\alpha$ x-rays. In the infinite-layer film, all four reflections are visible, with the 004 peak sitting at the end of the range accessible with our goniometer.

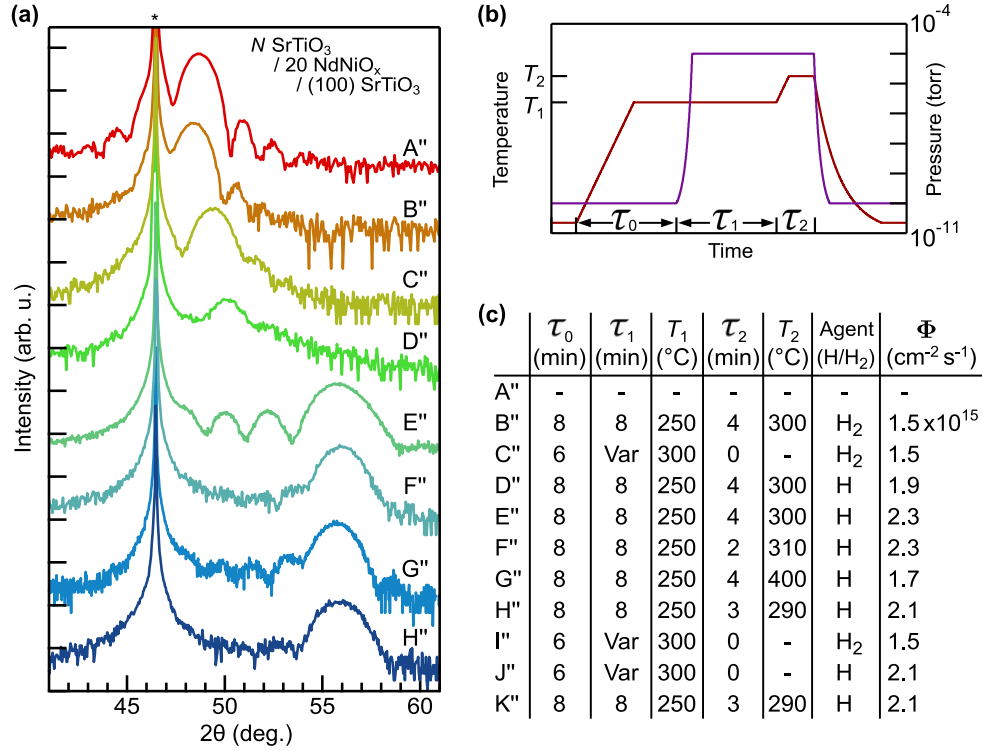


FIG. S8. Conditions used for H and H₂ reduction of films during experiments exploring the effect of the SrTiO₃ cap on reduction. (a) Replica of Fig. 7(a) from the main text with samples labeled. (b) Cartoon of a generic three-step ($\tau_2 \neq 0$) or two-step ($\tau_2 = 0$) reduction. (c) Table of reduction conditions used in the preparation of samples in (a) as well as in Figs. S9, S10, and S11.

B. Reduction Effects on the Film Surface

In this section we present additional data concerning the effects of molecular and atomic hydrogen on the film surface. In Fig. S8 we present the details of the reduction program used for samples in Fig. 7 (samples A''-G'') of the main text as well as those presented later in this section (samples I'', J''). Of these, several samples were subjected to several sequential single-step reduction cycles ($\tau_2 = 0$) with variable times, performing RHEED measurements between cycles. These include sample C'', which was reduced in four increments of 15, 15, 15, and 45 minutes (90 min total), sample I'' in four increments of 15, 30, 30, and 15 minutes (90 min total), and J'' in three increments of 15, 15, and 30 minutes (60 min total). Fluxes are quoted in atoms/cm²/sec for samples reduced with atomic hydrogen and in molecules/cm²/sec for those reduced with molecular hydrogen only. In all cases a consistent hydrogen flow rate of 0.72 sccm was used (giving a chamber pressure of $\sim 9.5 \times 10^{-6}$ torr) and the atomic hydrogen flux was adjusted by tuning the cracker temperature.

In Figs. S9 and S10 we detail two additional progressive annealing experiments. Figure S9 shows a sample with a 2 u.c. thick SrTiO₃ cap annealed in molecular hydrogen. As can be seen in the RHEED images, the molecular hydrogen has little-to-no impact on the SrTiO₃ surface, even for long exposure times. Similar to the uncapped sample shown in the main text, molecular hydrogen is insufficient to produce the infinite-layer phase (under these conditions) and instead an oxygen-deficient perovskite phase is visible in the XRD, with out-of-plane lattice parameter $c \sim 3.69$ Å, following 90 minutes of exposure. Figure S10 shows a sample that was exposed to atomic hydrogen in progressive steps. Similar to the sample presented in the main text, the RHEED images indicate a rapid degradation of the film surface and the presence of other phases (faint rings and additional spots). Even after a relatively long exposure, 60 minutes, the majority of the film remains an oxygen-deficient perovskite ($c \sim 3.69$ Å) without any indication of formation of the infinite-layer phase, evidenced by the XRD patterns in Fig. S10(b).

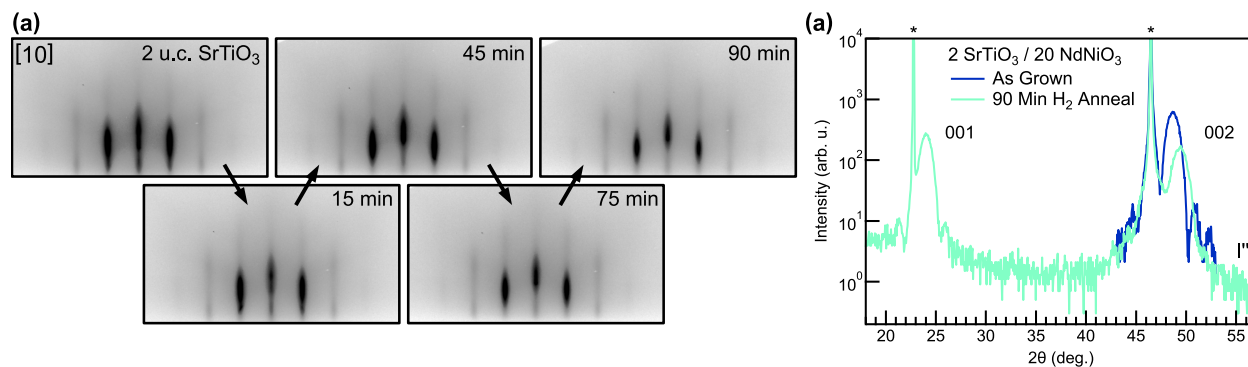


FIG. S9. Molecular hydrogen reduction of a 20 u.c. thick NdNiO₃ / SrTiO₃ film capped with 2 u.c. of SrTiO₃. (a) RHEED images along the [10] azimuth of a film exposed to H₂, at a temperature of 300 °C, for repeated intervals accumulating to 90 minutes total. (b) XRD measurements of the same film before and after the 90 minutes of total reduction time. (*) indicates reflections from the (001) oriented SrTiO₃ substrate.

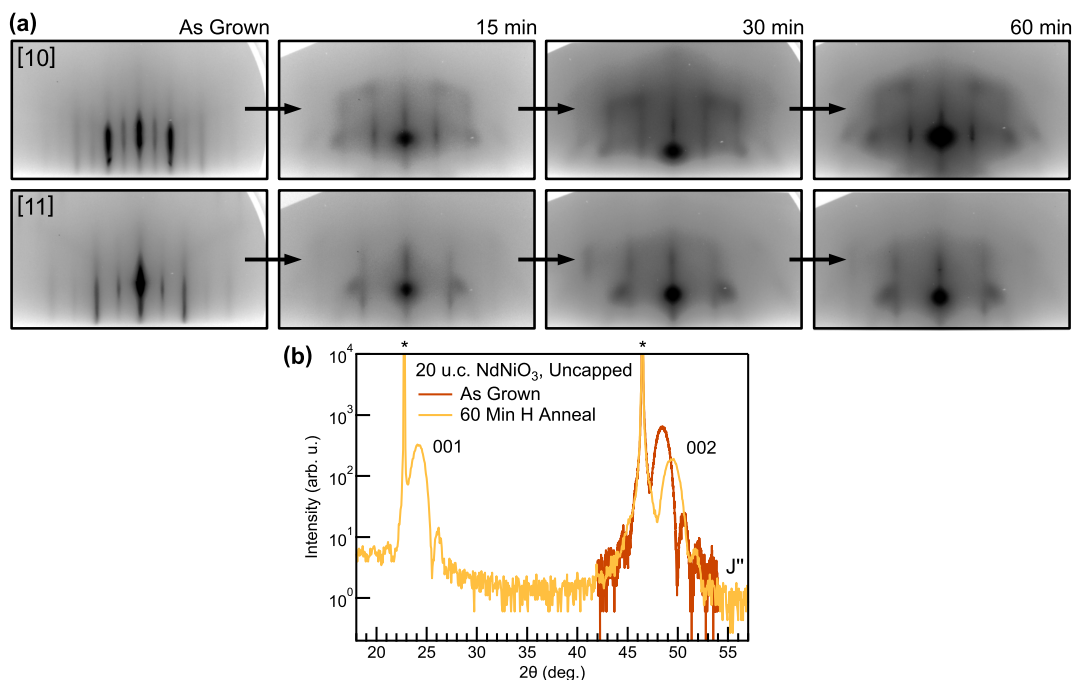


FIG. S10. Effects of atomic hydrogen reduction on an uncapped, 20 u.c. thick NdNiO₃ / SrTiO₃ film. (a) RHEED images along the [100]_{pc} and [110]_{pc} azimuths of an uncapped film; images are taken of the as grown film surface as well as after 15, 30, and 60 minutes of atomic hydrogen exposure time at a sample temperature of 300 °C. (b) XRD measurements of the same film before and after the 60 minute exposure. (*) indicates reflections from the (001) oriented SrTiO₃ substrate.

Finally, we discuss the effects of amorphous capping layers on the reduction of 20 u.c. NdNiO₃/SrTiO₃ films using atomic hydrogen. X-ray diffraction measurements showing the 001 and 002 peak regions for two films with amorphous caps are provided in Fig. S11(a). For both films, the capping layer was deposited in a background pressure of 2×10^{-6} torr of distilled O₃ with the sample at room temperature. For sample H'' the capping layer was deposited with Sr and Ti shutters opened simultaneously (codeposition) and for sample K'' the shutters were opened sequentially (shuttered deposition); in both cases no streaks, spots, or rings were visible in RHEED after deposition of the SrTiO₃ layers. The thickness of both capping layers was 1.2 nm – equivalent to 3 u.c. of SrTiO₃ – and the subsequent reductions, using the same conditions, appear to progress similarly based on the XRD measurements in Fig. S11(a). The obvious difference in XRD patterns between those samples reduced (using atomic hydrogen) with an amorphous cap (H'' and K'') versus those reduced with no cap (D'' and J'') illustrate the importance of the overlayer in facilitating

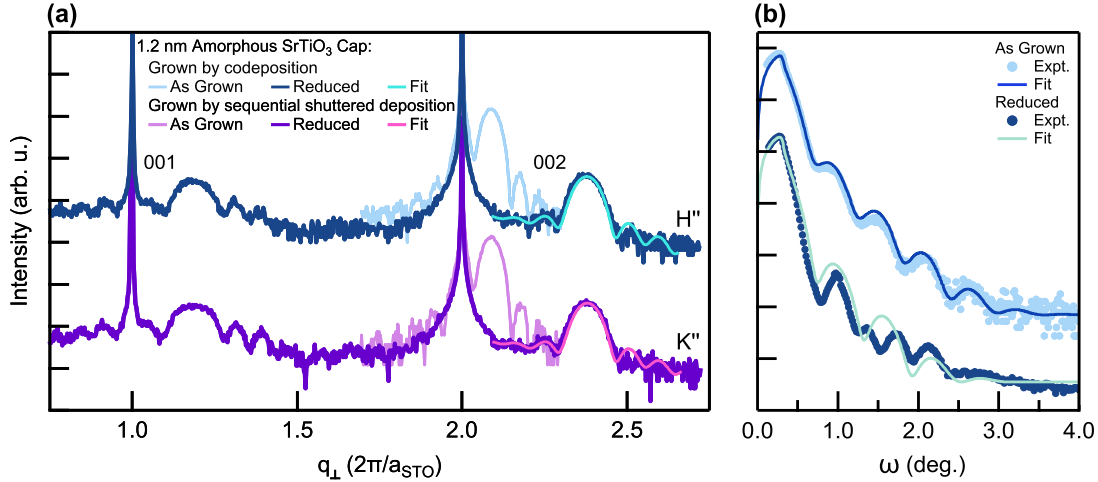


FIG. S11. Atomic hydrogen reduction of 20 u.c. thick $\text{NdNiO}_3 / \text{SrTiO}_3$ films capped with 1.2 nm of amorphous SrTiO_3 . (a) XRD of nickelate films as grown (light) and after capping and reduction (dark); capping layers were grown using either simultaneous codeposition of Sr and Ti (blue) or sequential shuttered deposition (purple) at room temperature. 002 peaks of the reduced films are fit with an N -slit interference pattern (teal, pink) to extract the coherent thickness. (b) Low-angle XRR of one of the samples before and after capping/reduction (dots) and corresponding best fits (lines) using a three slab model.

the reduction even in the absence of epitaxial stabilization.

We do note, however, that the quality of the amorphous SrTiO_3 capped samples are somewhat reduced compared to those with a crystalline cap. Fitting of the XRD patterns of both the reduced films with an N -slit interference pattern,

$$I \propto \frac{1}{N} \frac{\sin^2(Naq/2)}{\sin^2(aq/2)},$$

gives a Scherrer thickness of only 4.43 nm, *i.e.* $N \sim 13.5$, indicating that the coherent crystalline region does not extend across the entirety of the film thickness. Additionally, the x-ray reflectivity, Fig. S11(b), of the reduced film cannot be accurately fit using a three-slab model ($\text{SrTiO}_3/\text{NdNiO}_3/\text{SrTiO}_3$) as was done for the crystalline film in Fig. 5(d) of the main text. The best-fit (green) for this reflectivity curve gives a roughness for the NdNiO_2 layer, 3.2 nm (compared to that of the as grown film, 0.48 nm), and a thickness of 5.6 nm (intermediate to the Scherrer thickness of 4.4 nm and the expected thickness of 6.5 nm). These results are consistent with the capping layer providing some measure of epitaxial support during the reduction process, which is absent in those films with an amorphous cap, and a fraction of the film either forms a defect phase or decomposes – as reported previously in CaH_2 reduced films [5]. We cannot rule out, however, that the observed differences between the crystalline and amorphous SrTiO_3 capped films result from differences in transport of the reactants (*e.g.* H or O_2) through the different matrices. We emphasize, however, that the role of the capping layer, at least in atomic hydrogen reduction experiments, clearly goes beyond that of epitaxial stabilization. In the XRD patterns of uncapped films, D'' and J'', the effect of the reduction is *not* to cause decomposition of the entire thickness of the film, but rather to form a polycrystalline scale on the surface and to hamper further reduction – as evidenced by the minor 002 peak shifts observed in XRD. This is in contrast with the more modest observed differences between crystalline capped (Samples F'', G'') and amorphous capped (Samples H'', K'') films which all exhibit similar 002 peak positions.

-
- [1] E. Breckenfeld, Z. Chen, A. R. Damodaran, and L. W. Martin, Effects of nonequilibrium growth, nonstoichiometry, and film orientation on the metal-to-insulator transition in NdNiO₃ thin films, *ACS Applied Materials and Interfaces* **6**, 22436 (2014).
- [2] D. Preziosi, A. Sander, A. Barthélémy, and M. Bibes, Reproducibility and off-stoichiometry issues in nickelate thin films grown by pulsed laser deposition, *AIP Advances* **7**, 015210 (2017).
- [3] T. Yamanaka, A. N. Hattori, L. N. Pamasi, S. Takemoto, K. Hattori, H. Daimon, K. Sato, and H. Tanaka, Effects of Off-Stoichiometry in the Epitaxial NdNiO₃ Film on the Suppression of Its Metal-Insulator-Transition Properties, *ACS Applied Electronic Materials* **1**, 2678 (2019).
- [4] G. A. Pan, Q. Song, D. Ferenc Segedin, M. C. Jung, H. El-Sherif, E. E. Fleck, B. H. Goodge, S. Doyle, D. Córdoba Carrizales, A. T. N'Diaye, P. Shafer, H. Paik, L. F. Kourkoutis, I. El Baggari, A. S. Botana, C. M. Brooks, and J. A. Mundy, Synthesis and electronic properties of Nd_{n+1}Ni_nO_{3n+1} Ruddlesden-Popper nickelate thin films, *Physical Review Materials* **6**, 055003 (2022).
- [5] K. Lee, B. H. Goodge, D. Li, M. Osada, B. Y. Wang, Y. Cui, L. F. Kourkoutis, and H. Y. Hwang, Aspects of the synthesis of thin film superconducting infinite-layer nickelates, *APL Materials* **8**, 041107 (2020).
- [6] Y. Li, W. Sun, J. Yang, X. Cai, W. Guo, Z. Gu, Y. Zhu, and Y. Nie, Impact of Cation Stoichiometry on the Crystalline Structure and Superconductivity in Nickelates, *Frontiers in Physics* **9**, 1 (2021).
- [7] K. Lee, B. Y. Wang, M. Osada, B. H. Goodge, T. C. Wang, Y. Lee, S. Harvey, W. J. Kim, Y. Yu, C. Murthy, S. Raghu, L. F. Kourkoutis, and H. Y. Hwang, Linear-in-temperature resistivity for optimally superconducting (Nd,Sr)NiO₂, *Nature* **619**, 288 (2023).
- [8] J. Sun, C. T. Parzyck, J. H. Lee, C. M. Brooks, L. F. Kourkoutis, X. Ke, R. Misra, J. Schubert, F. V. Hensling, M. R. Barone, Z. Wang, M. E. Holtz, N. J. Schreiber, Q. Song, H. Paik, T. Heeg, D. A. Muller, K. M. Shen, and D. G. Schlom, Canonical approach to cation flux calibration in oxide molecular-beam epitaxy, *Physical Review Materials* **6**, 033802 (2022).
- [9] P. D. C. King, H. I. Wei, Y. F. Nie, M. Uchida, C. Adamo, S. Zhu, X. He, I. Božović, D. G. Schlom, and K. M. Shen, Atomic-scale control of competing electronic phases in ultrathin LaNiO₃, *Nature Nanotechnology* **9**, 443 (2014).
- [10] W. Wei, K. Shin, H. Hong, Y. Shin, A. S. Thind, Y. Yang, R. F. Klie, F. J. Walker, and C. H. Ahn, Solid state reduction of nickelate thin films, *Physical Review Materials* **7**, 013802 (2023).